Motion and deformation of capsules flowing through a corner in the inertial and non-inertial regimes

Damien P. Huet, Antoine Morente, and Guodong Gai
Department of Mathematics, University of British Columbia, 1984 Mathematics Road, Vancouver, British Columbia V6T 1Z2, Canada

Anthony Wachs*
Department of Mathematics, University of British Columbia, 1984 Mathematics Road, Vancouver, British Columbia V6T 1Z2, Canada
and Department of Chemical and Biological Engineering, University of British Columbia, 2360 E Mall, Vancouver, British Columbia V6T 1Z3, Canada

(Received 9 May 2023; accepted 1 April 2024; published 3 May 2024)

We investigate the inertial and non-inertial dynamics of three-dimensional elastic capsules flowing through a square channel presenting a sharp corner. Our study analyzes the trajectory, surface area, velocity, and membrane stress of the capsules in the case of a single capsule, a system of two interacting capsules, and a train of ten capsules released upstream of the corner. The channel Reynolds number Re ranges from 0.01 to 50 and the Capillary number Ca, which measures the ratio of the viscous and elastic stresses, ranges from 0.075 to 0.35. We find that in the inertial regime, the membrane stretch and stress increase dramatically as compared to the non-inertial case, and that the velocity overshoot inside the corner is also enhanced. The maximum capsule deformation is observed to depend nearly linearly on Ca and Re. Additionally, we report a repelling mechanism between two confined capsules when their initial interspacing distance d is smaller than a critical value d_c. The deformation of the leading capsule is found to be mitigated by the presence of the following capsule. In the case of multiple capsules flowing through the corner, we observe that the increase in the maximum surface area of the trailing capsules eventually saturates at the tail of the train. Moreover, we find that the corner tends to separate the capsules regardless of their upstream interspacing distances d. This study contributes to the elaboration of practical guidelines for controlling capsule breakup and predicting throughput in both inertial and non-inertial microfluidic experiments.

DOI: 10.1103/PhysRevFluids.9.053601

I. INTRODUCTION

Membrane-enclosed fluid objects, or capsules, are everywhere in natural and industrial processes, from red blood cells (RBCs), circulating tumor cells (CTCs), or flowing eggs in biology to encapsulated substances in the pharmaceutical, cosmetic, and food industries [1]. The study of microcapsules, in particular, is of primary importance in a variety of biological applications, such as sorting and enriching solutions of biological microcapsules, e.g., to segregate RBCs or CTCs, as well as efficiently manufacturing capsules enclosing an active substance in the field of targeted drug delivery [2,3]. In the past decade, microfluidic devices have been shown to accomplish a variety of tasks including cell segregation based on size and deformability [4–7], concentration enrichment

*wachs@math.ubc.ca

[8–10], and cell characterization [11–13]. Moreover, the increase in computing power has recently allowed numerical studies to contribute to the design of microfluidic devices. For example, Zhu *et al.* [4] numerically investigated an original microchannel geometry consisting of a semicircular pillar located at the center of a microchannel: their study showed that this design can efficiently segregate cells based on membrane deformability. Recently, experiments were conducted using their microfluidic design and concluded that it can indeed sort cells based solely on membrane stiffness, with relatively high efficacy [5]. With regards to cell characterization, Gubspun *et al.* [11] proposed a method to determine capsule properties such as the membrane shear modulus by comparing the experimental and numerical "parachute" shape of capsules in a straight microchannel. While the majority of microfluidic investigations operate in Stokes conditions, in recent years the design and study of inertial microfluidic devices has risen due to their ability to accurately segregate capsules by size and to extract them from their solvent [7,14]. Inertial focusing in microfluidic devices typically relies on a spiral-shaped channel concentrating heavier capsules to the outer, lower-curvature edge of the channel, while lighter capsules concentrate closer to the inner, higher-curvature edge. A smooth geometry such as a spiral-shaped channel usually does not induce a high strain nor stress on a suspended capsule even in inertial regimes; however, little is known about the strains and stresses induced by commonly encountered sharp geometries such as forks and corners on a capsule flowing in the presence of inertia. Moreover, the effect of such sharp geometries on the hydrodynamic interactions of a train of several capsules in inertial regimes is also an open question. More insight in these directions is of practical interest in the design and operation of inertial microfluidic devices because (i) the devices should not compromise the mechanical integrity of the capsules, i.e., it is critical to avoid capsule breakup, and (ii) cell-sorting processes typically operate in very dilute regimes to avoid capsule interactions, while a better understanding of such interactions would allow to operate these devices at a moderate to high concentration optimizing efficacy and throughput.

In the past four decades, a significant research effort has been invested into the modeling and the study of capsule deformations in non-inertial regimes, primarily because this regime is encountered in microcirculation such as capillary vessels and in traditional microfluidic devices. Using formalism from the thin-shell theory [15], Barthés-Biesel and Rallison first published an analytical solution for the time-dependant deformation of an elastic capsule in an unbounded, creeping shear flow in the limit of small deformations [16]. Over a decade later, Pozrikidis was able to go beyond the assumption of small deformations using a boundary integral method (BIM) [17]. The same method was used to consider finite deformations of sheared capsules which inner and outer fluid viscosities differ [18], as well as to study the contribution of bending stresses [19], allowing to consider capsules suspended in an unbounded shear flow [20]. Besides unbounded geometries, Hu *et al.* [21] considered an initially spherical capsule flowing through a square channel of width similar to the capsule diameter: the originality of their work is that they performed experiments and showed remarkable agreement between the measured and the computed capsule shape. Concomitantly, Park and Dimitrakopoulos [22] studied the deformation of a capsule with nonunity viscosity ratio flowing through a sharp constriction. More recently, Balogh and Bagchi [23–25] used a front-tracking method (FTM) to analyze the motion and deformation of RBCs through complex geometries resembling capillary vessels found in human microcirculation.

In microfluidic applications, inertia is often negligible due to the small length scales involved. However, in recent studies, inertial particle microfluidics (IPMF) serves as an emerging technology for the manipulation and separation of microparticles and biological cells with high precision and efficiency [26,27]. IPMF has the potential to speed up labor-intensive nondestructive diagnosis procedures such as cell sorting and has been employed in the microbiology [28–30] and biotechnology [31,32] industries. Because the flow velocities in inertial microfluidics are significantly larger than their counterparts in non-inertial microfluidics [33], the aforementioned analytical theory for small deformations as well as the popular BIM both fall short of accounting for the convective term in the fluid momentum equation. Doddi and Bagchi [34] first studied inertial capsules in the context of two interacting capsules in a shear flow using the FTM. They showed in particular that the two capsules engage in spiraling motions at sufficiently high inertia. The inertial motion of a deformable

capsule was then studied in straight microchannels [35,36], where several equilibrium positions are found away from the channel centerline, along the cross-section diagonals. The primary inertial forces at play include: (i) the wall repulsion force, which drives particles away from channel walls; (ii) shear-gradient lift forces, typically directing particles towards areas of higher shear; and (iii) drag forces within secondary flow fields, which arise due to curved streamlines [27]. With regards to curved channels, Ebrahimi and Bagchi [37] recently investigated the migration of a single capsule over an impressive amount of varying parameters: the channel Reynolds number, the capsule deformability, as well as the aspect ratio and curvature of the channel were all varied independently. Their study shows that for sufficiently high inertia, exactly two focusing locations appear near the centers of the vortices of the secondary flow, known as Dean vortices. However no mention of the membrane internal strains and stresses is found in their work, as their goal was not to investigate the capsule integrity in such flows.

While straight and curved microchannels are essential components of microfluidic devices, such simple geometries do not account for the numerous junctions, corners and coils commonly found in these devices. To bridge this gap, Zhu and Brandt [38] investigated the non-inertial motion and the deformation of a single elastic capsule in a sharp corner. They showed that the capsule follows the streamlines of the undisturbed flow regardless of membrane deformability. Due to lubrication forces, the capsule velocity decreases when approaching the corner, reaches a minimum along the corner diagonal, and rises back to its steady state with an overshoot increasing with deformability. Similarly, the surface area of the capsule reaches a maximum inside the corner and relaxes back to its steady value with an undershoot more pronounced as deformability is increased. Also reported in their study is the maximum stress in the capsule membrane, which can be used to assess mechanical integrity and characterize the cell mechanical properties. They find that the maximum stress deviation increases and shifts from the front to the top of the capsule with increasing deformability. Wang *et al.* [8,9] later considered the inertial and non-inertial path selection of a single capsule through Y and T junctions, both typically encountered in microfluidic geometries. They observe that at high inertia, the capsule does not necessarily favor the daughter branch with the largest flow rate, and that this effect is more pronounced for stiff membranes (corresponding to a low capillary number). Recently, Lu *et al.* [10] investigated the interaction and path selection of capsules in a T junction at moderate inertia, with the goal of enriching capsule solutions. When considering a pair of capsules, they show that the leading capsule is weakly affected by the presence of a trailing capsule, but that the reverse is not true. They find that the trailing capsule enters a different branch depending on the initial interspacing distance and on the flow rate split ratio between the two daughter branches of the T junction. They then consider a train of capsules and find two distinct regimes: (i) the interspacing distance is low and the capsule interaction is high, resulting in an unsteady regime and affecting the trajectories of the capsules, and (ii) the interspacing distance is large and the capsule interaction is low, leaving the capsule trajectories identical to that of a single capsule. Interestingly, they report that the critical interspacing distance between two capsules plotted against the flow rate split ratio of the daughter branches results in a master curve independent of membrane deformability, capsule size, and Reynolds number.

In this study, we investigate the inertial and non-inertial motion and the interaction of deformable capsules flowing through a sharp corner, which is a very common geometry in microfluidic devices. As the efficiency of these devices is defined in terms of the capsules throughput, which can be optimized by increasing the flow rate as well as the concentration of capsules, our objective is twofold: first, we aim to quantify the effet of inertia on the deformation of a single capsule in a microfluidic-relevant geometry, second, we seek to describe the hydrodynamic interactions and deformation differences between leading and trailing capsules when a pair and a train of capsules are considered. The rest of this paper is organized as follows. In Sec. II, we describe the governing equations as well as the flow configuration and the considered parameter space. In Sec. III, we give an overview of our numerical method and we investigate the impact of the inlet length. We analyze the motion of a single capsule in Sec. IV, both in the non-inertial and in the inertial regimes. Section V is devoted to the analysis of binary interactions of a pair of capsules, where the influence

of the initial interspacing distance is investigated. In Sec. VI, we consider a train of ten capsules flowing through the corner and we discuss the velocity and deformation discrepancies between the leading and trailing capsules. Finally, we conclude in Sec. VII.

The documented source code allowing to reproduce all of the simulations and figures presented in this study is freely available online [39].

II. GOVERNING EQUATIONS AND PROBLEM STATEMENT

The capsule membrane Γ is assumed infinitely thin and is surrounded by an incompressible, Newtonian fluid of constant viscosity and density. In all of this study, the capsule inner and outer fluids are assumed identical: in particular their viscosity ratio is unity. The fluid is described by the mass and momentum conservation equations:

$$\tilde{\nabla} \cdot \tilde{\boldsymbol{u}} = 0, \tag{1}$$

$$\frac{\partial \tilde{\boldsymbol{u}}}{\partial \tilde{t}} + \tilde{\boldsymbol{u}} \cdot \tilde{\nabla} \tilde{\boldsymbol{u}} = \frac{1}{\tilde{\rho}} \tilde{\nabla} \tilde{p} + \tilde{\nu} \tilde{\Delta} \tilde{\boldsymbol{u}} + \frac{1}{\tilde{\rho}} \tilde{\boldsymbol{f}}_{\boldsymbol{b}}, \tag{2}$$

where $\tilde{\boldsymbol{u}}$ is the velocity field, $\tilde{p}$ is the pressure field, $\tilde{\rho}$ is the density, $\tilde{\nu} = \tilde{\mu}/\tilde{\rho}$ is the kinematic viscosity, $\tilde{\mu}$ is the dynamic viscosity, and $\tilde{\boldsymbol{f}}_{\boldsymbol{b}}$ is a body term accounting for the action of the membrane on its surrounding fluid. The dimensional quantities are denoted by the $\sim$ symbol. The membrane exhibits elasticity and bending resistance, and its action on the fluid is local, resulting in the following expression for $\tilde{\boldsymbol{f}}_{\boldsymbol{b}}$:

$$\tilde{\boldsymbol{f}}_{\boldsymbol{b}} = (\tilde{\boldsymbol{f}}_{\text{elastic}} + \tilde{\boldsymbol{f}}_{\text{bending}}) \tilde{\delta}(\tilde{\boldsymbol{x}} - \tilde{\boldsymbol{x}}_{\boldsymbol{\Gamma}}), \tag{3}$$

where $\tilde{\delta}(\tilde{\boldsymbol{x}} - \tilde{\boldsymbol{x}}_{\boldsymbol{\Gamma}})$ is a Dirac distribution that is nonzero on the surface of the membrane.

The shear and area-dilatation membrane stresses are described using the thin-shell theory, and are briefly summarized here. The interested reader is referred to Green and Adkins [15] as well as to the analytical study of Barthés-Biesel and Rallison [16] for more details. We adopt a neo-Hookean law [15], which surface strain-energy function is expressed as

$$\tilde{W}_s^{\text{NH}} = \frac{\tilde{E}_s}{2} \left(\lambda_1^2 \lambda_2^2 + \frac{1}{\lambda_1^2 \lambda_2^2} \right), \tag{4}$$

where $\lambda_{1,2}$ are the principal stretches in the two tangential directions, and $\tilde{E}_s$ is a shear modulus. The principal stresses $\tilde{\sigma}_{1,2}$ are given by

$$\tilde{\sigma}_i = \frac{1}{\lambda_j} \frac{\partial \tilde{W}_s^{\text{NH}}}{\partial \lambda_i}, \quad i, j \in \{1, 2\}, \quad i \neq j. \tag{5}$$

The bending stresses for biological membranes are governed by Helfrich's bending energy $\tilde{\mathcal{E}}_b$ [40,41]:

$$\tilde{\mathcal{E}}_b = \frac{\tilde{E}_b}{2} \int_{\Gamma} (2\tilde{\kappa} - \tilde{\kappa}_0)^2 dS, \tag{6}$$

where $\tilde{E}_b$ is the bending modulus, $\tilde{\kappa}$ is the mean curvature and $\tilde{\kappa}_0$ is a reference curvature. Taking the variational formulation of Eq. (6) leads to the bending force per unit area $\tilde{A}$:

$$\tilde{\boldsymbol{f}}_{\text{bending}}/\tilde{A} = -2\tilde{E}_b [\Delta_s \tilde{\kappa} + 2(\tilde{\kappa} - \tilde{\kappa}_0)(\tilde{\kappa}^2 - \tilde{\kappa}_g + \tilde{\kappa}_0 \tilde{\kappa})] \boldsymbol{n}, \tag{7}$$

where $\tilde{\kappa}_g$ is the Gaussian curvature and $\boldsymbol{n}$ is the outer normal vector.

At $t = 0$, an initially spherical capsule of radius $\tilde{a}$ is placed in a square channel of width $\tilde{W} = 3\tilde{a}$ at a distance $\tilde{h}_0 = 30\tilde{a}$ from a sharp corner, as represented in Fig. 1. An average cross-section velocity $\tilde{U}_0$ is imposed at the inlet boundary, while the outflow boundary condition $\partial \tilde{\boldsymbol{u}}_n / \partial \boldsymbol{n} = 0$ is imposed at the outlet boundary. When several capsules are considered, we use the same initial

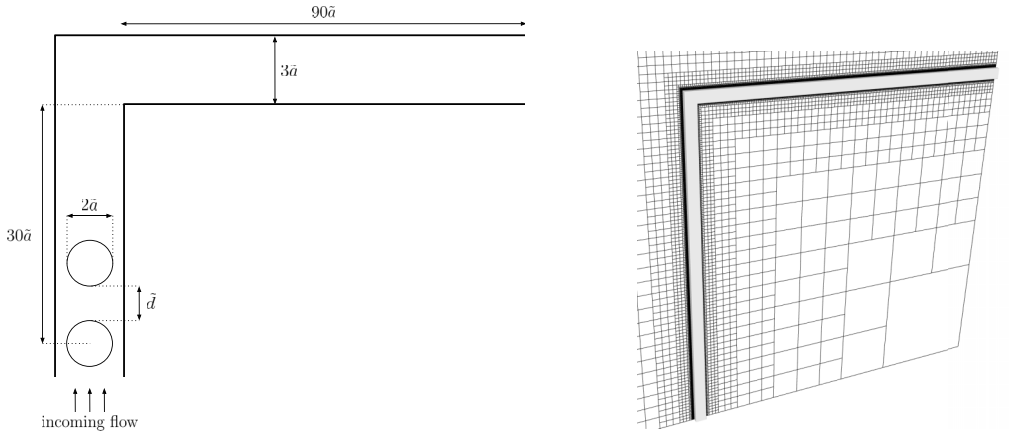

FIG. 1. (a) Schematic of the geometry of the fluid domain. The channel has a square cross-section of side length $3\tilde{a}$. (b) Visualization of the full channel and the computational grid over the symmetry plane of the channel

conditions as Lu *et al.* [10]: a trailing capsule is inserted in the simulation only after the centroid of its preceding capsule has advanced by a distance $\tilde{d}$. Our problem is governed by the dimensionless numbers:

(1) The channel Reynolds number $\mathrm{Re} = \tilde{\rho}\tilde{U}_0\tilde{W}/\tilde{\mu}$,

(2) The Capillary number $\mathrm{Ca} = \tilde{\mu}\tilde{U}_0\tilde{a}/\tilde{E}_s$, representing the ratio of viscous stresses over elastic stresses,

(3) The reduced bending stiffness coefficient $E_b = \tilde{E}_b/(\tilde{E}_s a^2)$,

(4) The confinement ratio $\beta = 2\tilde{a}/\tilde{W}$,

(5) The reduced initial gap between capsules $d_0 = \tilde{d}/2\tilde{a} - 1$.

In this study, the Reynolds number Re ranges from 0.01 to 50, the Capillary number Ca varies from 0.075 to 0.35, and the reduced initial gap d_0 is chosen from 0.125 to 1. The reduced bending stiffness E_b and the confinement ratio β are both kept constant, with $\beta = 2/3$ and $E_b = 5 \times 10^{-3}$ as proposed by Pozrikidis [42]. Here, a small confinement ratio can significantly enhance trajectory control, particularly in applications like cell sorting. In such a setup, the confinement effectively channels the cells, allowing for more accurate sorting based on their directed trajectories which is especially beneficial to a cell-sorting geometry situated downstream of the corner. The reference curvature $\tilde{\kappa_0}$ is equal to $-2.09/\tilde{a}$ in this study, as is common for some biological membranes [43,44]. In the rest of this study, we use the capsule radius $\tilde{a}$ as the characteristic length scale, and we define the characteristic time scale as the ratio of the capsule radius over the average cross-section velocity, i.e., $\tilde{T}_c = \tilde{a}/\tilde{U}_0$. By applying adaptive mesh refinement as depicted in Fig. 1(b), our simulation employs approximately 6.7 million Eulerian cells. Such a number of cells represents a significant reduction from the 8.6 billion Eulerian cells required by a conventional uniform Cartesian grid to maintain an equivalent resolution on the capsule membrane. The dimensionless time step magnitude $\Delta t = \Delta\tilde{t}/\tilde{T}_c$ varies between 10^{-4} and 5×10^{-4} depending the Reynolds number Re.

III. NUMERICAL METHOD AND VALIDATIONS

We use our adaptive front-tracking method (FTM) to solve the above equations: we provide below a brief overview of the numerical method, while an in-depth description is available in [45]. Equations (1) and (2) are solved using the finite volume method on an adaptive octree grid

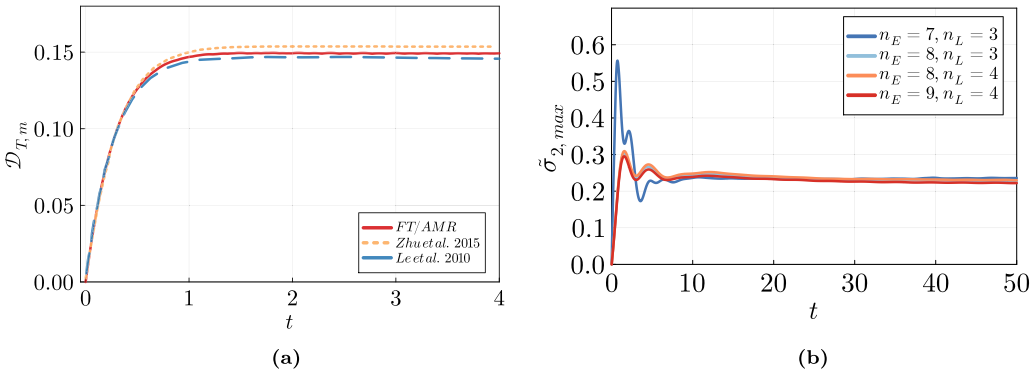

FIG. 2. (a) Taylor deformation factor $\mathcal{D}_{T,m}$ for an elastic capsule with Helfrich bending in a simple shear flow at Re = 0.01, $\dot{\gamma} = 1$, and Ca = 0.15; the numerical results of the current study are presented as a red line, in comparison with the data previously reported in the literature [38,49]; (b) convergence of the maximum tension $\tilde{\sigma}_{2,\max}$ with increasing grid resolution for a single capsule in a simple shear flow at Re = 10, $\dot{\gamma} = 1$, and Ca = 0.15.

using the open-source software Basilisk [46]. The membrane is discretized using an unstructured triangulation and Eq. (5) is solved using a linear finite element method, while Eq. (7) is solved using a paraboloid-fitting method. The membrane triangulation and the octree grid communicate by means of the immersed boundary method [47,48], where the Dirac distribution in Eq. (3) is regularized using a cosine-based formulation:

$$\tilde{\delta}(\boldsymbol{x_0} - \boldsymbol{x}) = \begin{cases} \dfrac{1}{64\tilde{\Delta}^3} \displaystyle\prod_{i=1}^{3} \left(1 + \cos\left(\frac{\pi}{2\tilde{\Delta}}(x_{0,i} - x_i)\right)\right) & \text{if} \quad |x_{0,i} - x_i| < 2\tilde{\Delta} \\ 0 \quad \text{otherwise} \end{cases}, \tag{8}$$

where $\boldsymbol{x_0} = [x_{0,1}\ x_{0,2}\ x_{0,3}]$ is the location of a Lagrangian node on the surface discretization of the membrane, and $\tilde{\Delta}$ is the local mesh size of the Eulerian octree grid.

To properly analyze the dynamics of the capsule as it flows through the corner, it is crucial to address the following key aspects in the numerical validation: (i) the chosen mesh resolution needs to be sufficiently fine to resolve the complex fluid-structure interactions within the wall-membrane lubrication layer, and (ii) the capsule should be in a steady state when entering the corner. As such, we conduct a grid convergence study with special focus on the resolution along the capsule membrane; and we perform a sensitivity analysis of our geometry with respect to the inlet length.

A widely employed metric for assessing the deformation of elastic capsules is the Taylor deformation factor $\mathcal{D}_{T,m}$ defined as follows:

$$\mathcal{D}_{T,m} = \frac{r_{\max} - r_{\min}}{r_{\max} + r_{\min}}, \tag{9}$$

where $r_{\max}$ and $r_{\min}$ represent the maximum and minimum distances, respectively, from the capsule membrane to its centroid. As an illustration of the numerical validation, we present the temporal evolution of $\mathcal{D}_{T,m}$ of an elastic capsule in a simple shear flow at Reynolds number Re = 0.01, shear rate $\dot{\gamma} = 1$ and capillary number Ca = 0.15 in Fig. 2(a). There is notable consistency between the numerical results of our adaptive solver and the values documented in the literature [38,49].

In addition, we analyze the convergence behavior of the maximum tension, denoted $\tilde{\sigma}_{2,\max}$, in a capsule subjected to a simple inertial shear flow at Re = 10, $\dot{\gamma} = 1$, and Ca = 0.15. In Fig. 2(b), the variables n_E and n_L represent the refinement levels for the Eulerian and Lagrangian meshes, respectively. Specifically, the Eulerian grid cell size is given by $\tilde{\Delta} = L_0/2^{n_E}$ within the fluid phase,

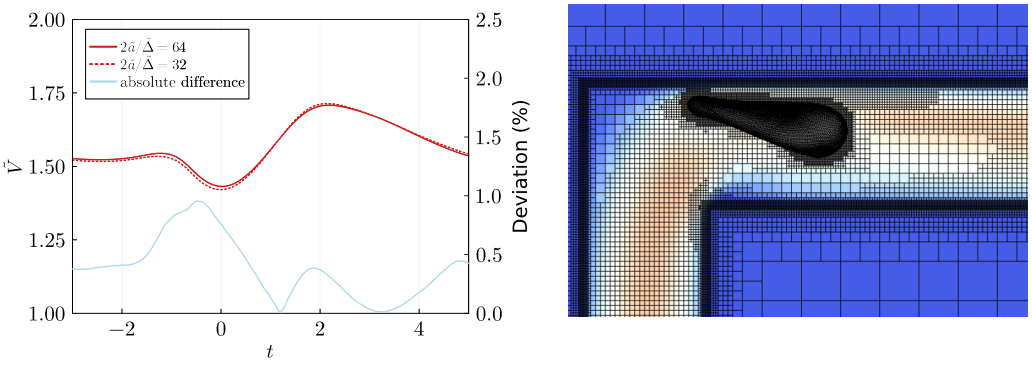

FIG. 3. (a) Centroid velocity of a capsule at Ca = 0.35 and Re = 50 for two grid resolutions: 32 grid cells per initial diameter (red dotted line) and 64 grid cells per initial diameter (red solid line). The blue curve denotes the deviation in the centroid velocities for these two grid resolutions; (b) corresponding shape and grid resolutions of the capsule and the flow field: blue means zero velocity and red means large velocity.

with L_0 is the length of the computational domain; and the capsule membrane is discretized into 20×4^{n_L} triangular elements. We denote by N_{pts} the number of grid cells per initial capsule diameter. As observed in Fig. 2(b), a grid refinement level of $n_E = 7$ ($N_{\text{pts}} = 16$) is insufficient to accurately capture the transient evolution of $\tilde{\sigma}_{2,\max}$, though it may yield acceptable steady-state values. When the Eulerian grid size $\tilde{\Delta}$ is reduced, the transient behaviors of the maximum tension $\tilde{\sigma}_{2,\max}$ obtained with different grid size almost supersimpose, converging to a consistent steady state for $n_E = 8$ and $n_E = 9$ ($N_{\text{pts}} = 32$ and 64, respectively). Upon comparing $n_L = 3$ (comprising 1280 surface elements) and $n_L = 4$ (consisting of 5120 surface elements), it is clear that an increase in Lagrangian mesh resolution does not significantly impact the convergence of $\tilde{\sigma}_{2,\max}$. For a more detailed examination of capsule deformation, particularly in corner regions, we will utilize $n_L = 4$ in subsequent computations. Extensive validation of the present numerical method on the curvature and stress was the focus of our previous study [45] and is therefore not presented here.

In the immersed boundary method, the finite support of the regularized Dirac distributions may extend outside of the fluid domain if the immersed object of interest becomes very close to the domain boundaries [9,10,50]. It is important to ensure that none of the supports of the regularized Dirac distributions extend outside of the fluid domain, i.e., we make sure that there always exist more than two grid cells between the membrane nodes and the domain boundaries. As such, we simulate the dynamics of a capsule for two different grid resolutions in the configuration where it is most deformed and is the closest to the channel wall, as shown in Fig. 3(b). Figure 3(a) shows the velocity of the capsule $\tilde{V}$ inside and downstream of the corner for Eulerian resolutions equivalent to 32 and 64 grid cells per initial capsule diameter, as well as the deviation of the velocities in these two configurations. The maximum velocity discrepancy is less than 1%, with an average discrepancy around 0.5% over the observed time frame. Additionally, in both scenarios, the width of the lubrication layer between the capsule tail and the upper corner wall remains over 3 grid cells. These observations show that a grid resolution equivalent to 32 cells per initial capsule diameter is adequate for converged solutions. Furthermore, the simulations are not compromised by immersed boundary stencils extending beyond the fluid domain, as this scenario does not occur.

Once released, the capsule transitions from a spherical shape to a stable equilibrium state as it migrates over a sufficient distance. It is crucial to ensure that this steady state is achieved before the capsule enters the corner. As such, we consider three initial distances $D_c = 15$, 30, and 60 in the most challenging configuration at Re = 50 and Ca = 0.35, i.e., the capsule is highly deformable and placed in a highly inertial flow. The inlet boundary is located at a distance of $90a$ away from

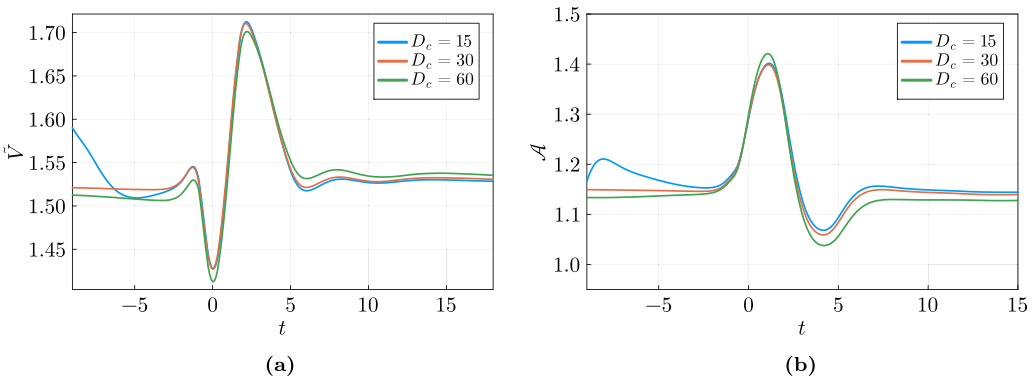

FIG. 4. Centroid velocity (a) and normalized surface area (b) of a capsule flowing through a corner from three distinct normalized release distances $D_c = 15$, 30, and 60, at $\mathrm{Re} = 50$ and $\mathrm{Ca} = 0.35$.

the corner and is therefore sufficiently far away from the capsule to not alter its response. The norm of the capsule centroid velocity $\tilde{V}$ and the reduced capsule surface area $\mathcal{A} = \tilde{\mathcal{A}}/4\pi\tilde{a}^2$ are shown in Fig. 4(a), where the origin of the reduced time t is chosen at the time the capsule reaches a minimum velocity $\tilde{V}_{\mathrm{min}}$. In Fig. 4(a) we remark that the capsule velocity $\tilde{V}$ at $D_c = 15$ decreases significantly before entering the corner: this is because the initially spherical capsule is located farther away from the channel walls and is therefore advected faster than when it has reached a steady shape. We observe that neither the capsule velocity shown in Fig. 4(a) nor the normalized surface area shown in Fig. 4(b) present a steady state before the capsule enters the corner in the case $D_c = 15$. Therefore a larger initial distance D_c should be used. When considering $D_c = 30$, both the velocity and the normalized surface area present steady values before the corner. Interestingly, inside and after the corner the capsule velocity and surface area almost overlap when the capsule is released 15 and 30 initial radii away from the corner, suggesting that the corner resets the dynamics of the capsule regardless of its previous state. The fact that steady values for the velocity and the surface area of the capsule are reached before the corner for $D_c = 30$ suggests that this initial release distance is suitable for the rest of this study. Unexpectedly, when the capsule is released from $D_c = 60$, it seems to no longer be in a steady motion as its velocity (respectively its normalized surface area) is slightly decreasing (respectively slightly increasing) before entering the corner. This suggests that in this challenging configuration, the relaxation of the capsule from a fixed spherical shape to a steady "parachute" shape occurs over very long time scales. However, the magnitude of the deviations between the capsule velocity and surface area in the cases $D_c = 30$ and 60 is at most 3%. As the capsule has already reached a pseudo-steady state by the time it enters the corner in the case of $D_c = 30$, and as the aforementioned discrepancies are small, we choose $D_c = 30$ in the rest of this study. Again, this short study of the impact of the initial release distance on the capsule dynamics was performed in our most challenging configuration as we considered our highest Reynolds number and highest Capillary number. The discrepancy between the cases $D_c = 30$ and 60 is less pronounced—sometimes nonexistent—for less deformable membranes and less inertial flows.

IV. MOTION AND DEFORMATION OF A SINGLE CAPSULE

We consider the motion of a single capsule through a square duct at $\mathrm{Ca} = 0.075, 0.15, 0.25, 0.35$ and $\mathrm{Re} = 0.01, 1, 25, 50$, extending the investigation carried out in a non-inertial framework by Zhu and Brandt [38]. To establish the influence of the increasing effect of inertia on the motion and the deformation of a single capsule, we first recall the overall dynamics of a capsule moving through a duct corner in the Stokes regime, as detailed in [38]. The capsule once released from its initial position moves along the center of the channel due to the symmetry of the flow far from the corner.

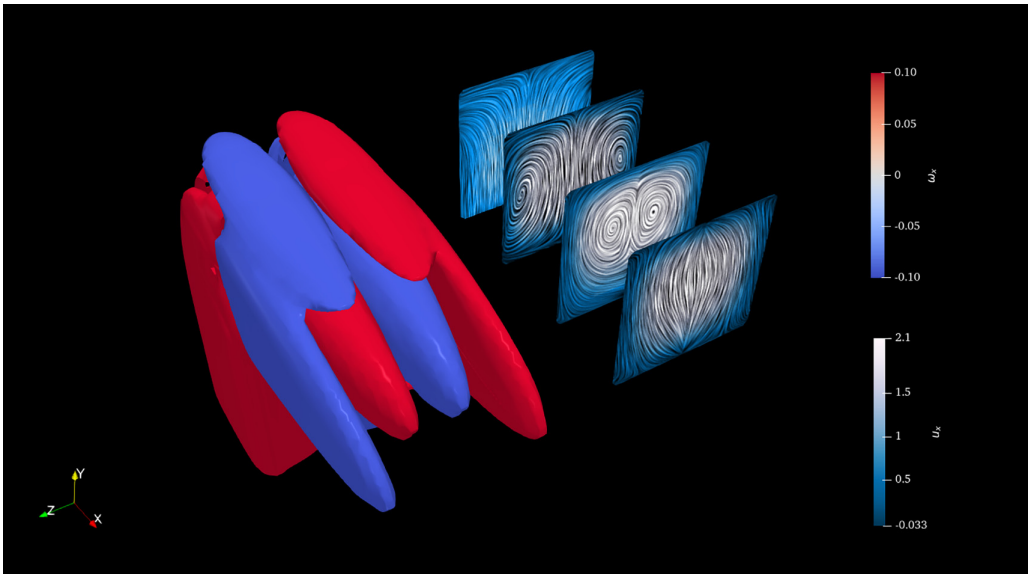

FIG. 5. Streamlines and vortex structures identified by isosurfaces of streamwise vorticity $\omega_x = \pm 0.1$ in the single-phase flow past the corner of a square channel at Re = 25.

While approaching the corner, the capsule velocity decreases until reaching a minimum in the corner region. The capsule experiences moderate to high deformation (depending on the Capillary number considered) due to the flow acceleration, and its velocity strongly increases; this phenomenon being referred to as the overshoot of velocity. Further away from the corner, the capsule moves in the downstream branch of the duct, relaxing to a steady state (shape and velocity), and moving along the center of the duct.

We investigate the influence of the Reynolds number Re and the Capillary number Ca on the dynamics and the deformation of the capsule, reporting the time evolution of its surface area $\mathcal{A}$ scaled by the initial surface area of the capsule $\tilde{\mathcal{A}}_{\text{sphere}} = 4\pi\tilde{a}^2$, as well as the velocity V of the capsule centroid scaled by its equilibrium velocity V_{eq} before the capsule enters the corner region. In the remainder of this study and unless otherwise stated, the time origin is chosen such that $t = 0$ when capsule velocity reaches a global minimum, i.e., $V_{\text{min}} = V(t = 0)$. We borrow this convention from Zhu and Brandt [38], as it corresponds to setting the time origin when the capsule is located in the heart of the corner.

A. Flow field through the corner

Recent studies show that the presence of curvature in a channel significantly affects the cross-streamline migration and focusing of deformable capsules over a wide range of Re [37,51]. When a fluid moves through a curved channel, the motion of the flow is redirected. Consequently, a secondary motion overlays the primary flow: a fluid particle initially located on the channel centerline moves outward, while a fluid particle initially located near the exterior wall flows inward. This action forms a pair of counterrotating recirculation regions known as Dean vortices.

In Fig. 5, we illustrate the streamlines and vortex structures, identified by isosurfaces of $\omega_x = \pm 0.1$ ($\omega_x = \tilde{a}\tilde{\omega}_x/\tilde{U}_0$), in the flow past the corner of our channel with square cross-section, with no capsule. This depiction clearly shows the presence of Dean vortices, which shift from the proximity of the lateral walls towards the upper wall of the channel as the fluid exits the corner. The counter-rotating vortices, colored in red ($\omega_x = 0.1$) and blue ($\omega_x = -0.1$) rapidly diminish in strength and eventually vanish when the flow stabilizes in the straight section of the secondary (downstream)

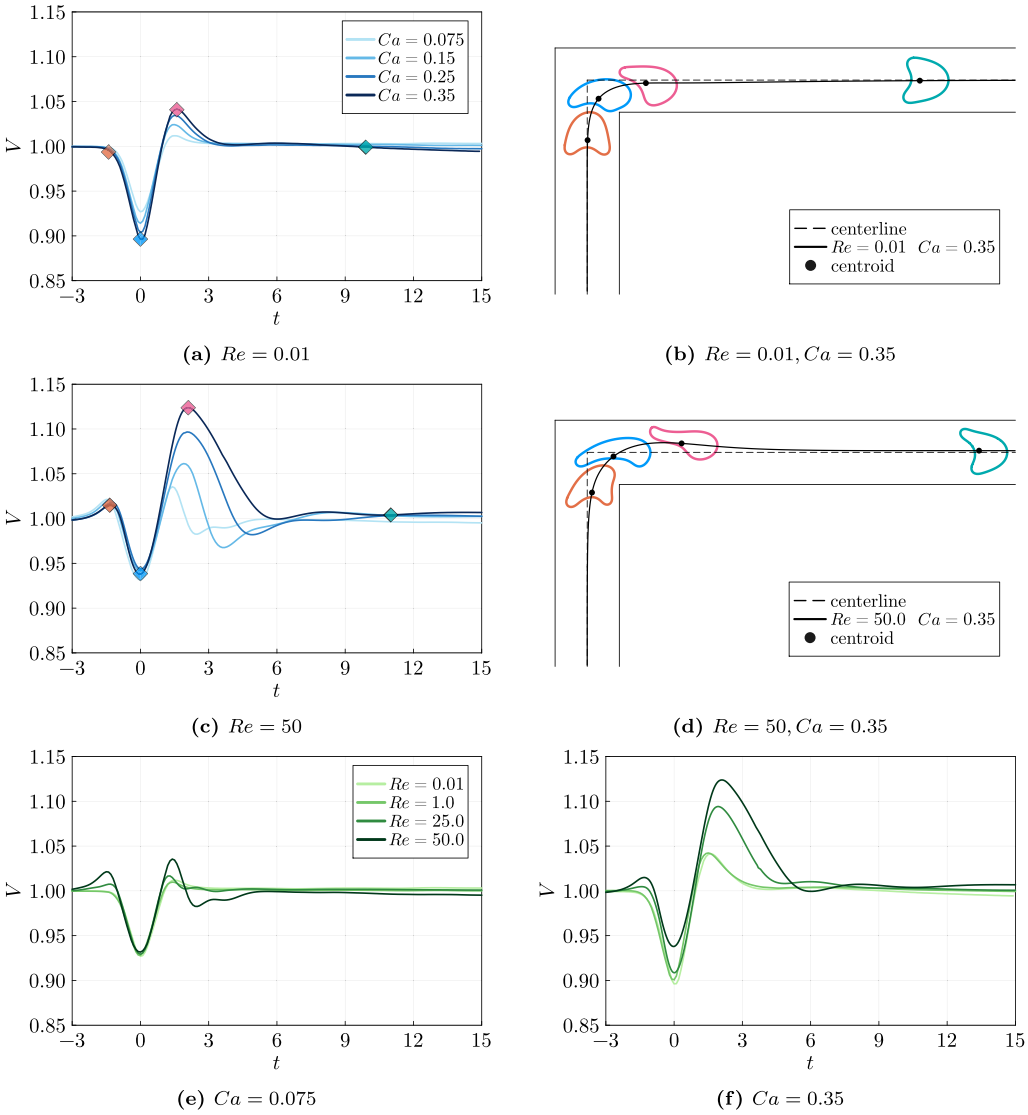

(a) $Re = 0.01$ **(b)** $Re = 0.01, Ca = 0.35$

(c) $Re = 50$ **(d)** $Re = 50, Ca = 0.35$

(e) $Ca = 0.075$ **(f)** $Ca = 0.35$

FIG. 6. (a), (c) Temporal evolution of the capsule centroid velocity V at Re $= 0.01$ and Re $= 50$; (b), (d) illustrations of the capsule outline at specific time instants highlighted in panels (a) and (c) at Ca $= 0.35$, respectively: onset of the decrease in velocity V (■), minimal V (■), maximum V (■), and relaxation to a steady state (■); (e), (f) temporal evolution of the capsule centroid velocity V at Ca $= 0.075$ and Ca $= 0.35$; the velocity evolution is normalized by V_{eq}, hence $V = V_{\text{eq}} = 1$ for $t \leqslant -3$ prior to capsule entering the corner in the panels (a), (c), (e), and (f).

channel along the x axis. In the sections that follow, we explore how the deformation and dynamics of the capsules are significantly influenced by the characteristics of the flow structures.

B. Influence of the Reynolds and Capillary numbers

To characterize the dynamics of the capsule, we analyze the temporal evolution of the centroid velocity V and the surface area $\mathcal{A}$ as it flows through the corner. Figures 6(a) and 6(c) present

the velocity of the capsule centroid at Re = 0.01 and 50 with Ca ranging from 0.075 to 0.35. To improve clarity, the capsule velocity V is normalized by its equilibrium velocity V_{eq} prior to entering the corner: $V \equiv (\tilde{V}/\tilde{U}_0)/(\tilde{V}_{eq}/\tilde{U}_0)$. We adopt this normalization in our subsequent discussions. We observe a general trend for the velocity evolution in Fig. 6(a): The capsule approaches the corner with a steady velocity $V = V_{eq} = 1$, then reaches a global minimum V_{min} and a global maximum V_{max} as it flows through the corner, and relaxes back to V_{eq} downstream of the corner. We illustrate the outline of the capsule at some critical time instants in Fig. 6(b). The color of the capsule outline corresponds to that of the highlighted points in Fig. 6(a). We see that the capsule velocity starts decreasing ( ) when it approaches the corner. The deceleration comes from the deflection of the streamlines and the blockage of the interior sharp corner. Then, the minimum velocity V_{min} ( ) is reached in the heart of the corner. Subsequently, the capsule velocity is accelerated and it migrates towards the centerline of the secondary channel. Its velocity reaches its maximum value V_{max} ( ) as it exits the corner area. During the acceleration (from capsule to capsule), we see that the capsule exhibits an elongated shape with its membrane located far away from the channel walls and is therefore less subject to the confinement effect. Finally, as the Dean vortices diminish, the capsule velocity also relaxes back to its equilibrium value ( ).

As the Reynolds number is increased to 50 in Fig. 6(c), major deviations from the non-inertial regime appear. First, as the capsule enters the corner zone, a local maximum appears in the capsule velocity as depicted in Fig. 6(c), which is independent of the Capillary number and is about 2% greater than V_{eq} at Re = 50. This local maximum of velocity is not present in the non-inertial case [Fig. 6(a)] because Dean vortices are the result of inertial conditions. At Re = 50, streamlines are already disturbed prior to the capsule entering the corner. We postulate that both this local maximum of velocity ( ) and the acceleration to V_{max} ( ) are due to the attractive effects of the Dean vortices in the inertial regime. Comparing Figs. 6(b) and 6(d), when the velocity begins to decrease, the capsule is closer to the side wall at Re = 50 than at Re = 0.01 and the capsule is more stretched and elongated at a higher Re. Additionally, the effects of Ca is more pronounced in the inertial regime. At Re = 50, the maximum velocity deviation of the capsule at Ca = 0.35 ($V_{max} - V_{eq} = 0.12$) is up to three times that of the capsule at Ca = 0.075 ($V_{max} - V_{eq} = 0.04$) as depicted in Fig. 6(c). Interestingly, after reaching the maximum, velocity undershoots are observed in Fig. 6(d) during the relaxation stage in the inertial regime. This happens when the capsule leaves the region of Dean vortices. With increasing Ca, the velocity undershoots become less pronounced, damped by the high deformability of the capsule.

From another point of view, we present the effects of Re on the capsule velocity at Ca = 0.075 and Ca = 0.35 in Figs. 6(e) and 6(f). For a fixed Ca = 0.075 in Fig. 6(e), we note that the curves corresponding to Re = 0.01 and Re = 1 practically overlap, indicating that the capsule motion in low inertial regimes is very similar to that in the non-inertial regime. Interestingly, in Fig. 6(e) at Ca = 0.075, V_{min} is observed to be independent of Re. In contrast, in the case of larger Ca, the minimum velocity of the capsule increases with Re. A difference of about 4% is observed for V_{min} as Re increases from 0.01 to 50 at Ca = 0.35. At Ca = 0.075, we observe an increase in the maximum velocity V_{max} of 3%, as Re varies from 0.01 to 50, as can be seen in Fig. 6(e). In contrast, at Ca = 0.35, there is a more pronounced change in V_{max}, which escalates from $V_{max} = 1.04$ at Re = 0.01 to $V_{max} = 1.12$ at Re = 50 in Fig. 6(f), amounting to an increase of 8%. This highlights the significant impact of Re on V_{max}, particularly at higher Ca. Lastly, the relaxation time of the capsule increases with increasing Re but does not depend as strongly on Ca.

The temporal evolution of the normalized capsule surface area $\mathcal{A}$ is shown in Fig. 7. We present the area evolution at Re = 0.01 and Re = 50 in Figs. 7(a) and 7(c). We observe that the surface area presents a maximum $\mathcal{A}_{max}$ around $t = 1$ before relaxing to its equilibrium value $\mathcal{A}_{eq}$. From Figs. 7(b) and 7(d), we see that the maximum area is reached when the capsule crosses the centerline of the secondary channel, and is located within the Dean vortices. The deformation becomes less important when the capsule exits the corner and decelerates due to the attraction of the vortices. We can see that the red capsule (which corresponds to the shape of maximum area) has a long tail at Re = 50 and Ca = 0.35, while the blue capsule (corresponding to the shape of minimum area)

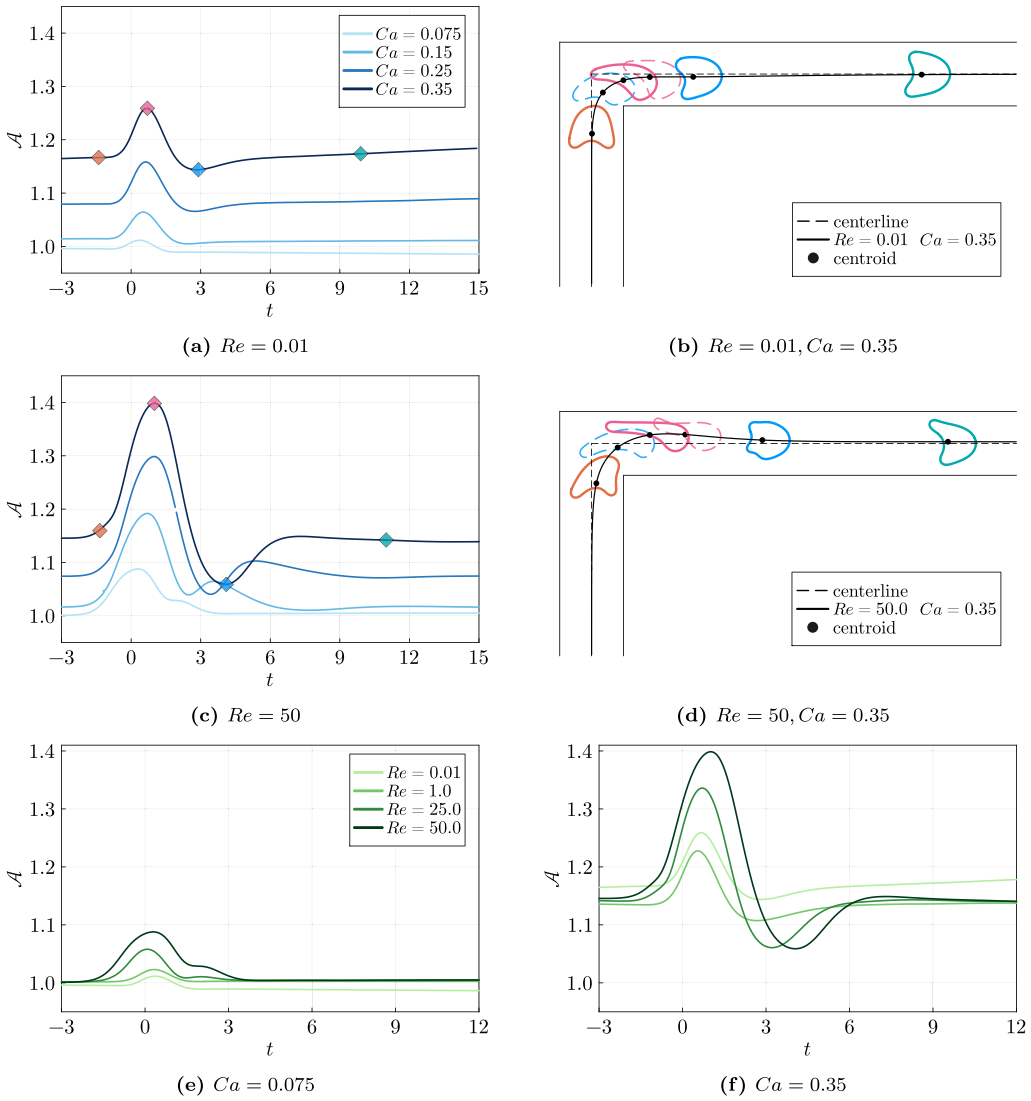

(a) $Re = 0.01$ **(b)** $Re = 0.01, Ca = 0.35$

(c) $Re = 50$ **(d)** $Re = 50, Ca = 0.35$

(e) $Ca = 0.075$ **(f)** $Ca = 0.35$

FIG. 7. (a), (c) Temporal evolution of the capsule surface area $\mathcal{A}$ at Re = 0.01 and Re = 50; (b), (d) Illustrations of the capsule outline at specific time instants highlighted in panels (a) and (c) at Ca = 0.35, respectively: onset of the increase in area $\mathcal{A}$ (■), maximum $\mathcal{A}$ (■), minimum $\mathcal{A}$ (■), and relaxation to a steady state (■); in comparison with the capsule outline with $V_{\min}$ (- - -) and $V_{\max}$ (- - -) (e), (f) Temporal evolution of the capsule surface area $\mathcal{A}$ at Ca = 0.075 and Ca = 0.35.

exhibits a more isotropic shape as it exits the vortical region. Unsurprisingly, Figs. 7(a) and 7(c) confirm that a large Ca, i.e., a highly deformable capsule, results in a greater surface area than for lower Ca. The normalized equilibrium area $\mathcal{A}_{\text{eq}}$ increases with Re and presents a significant increase with Ca. The magnitude of $\mathcal{A}_{\max}$ also increases with Ca. Moreover, when large Ca is considered, the time evolution of the capsule surface area presents some undershoots that are more pronounced as Re is increased in Fig. 7(c). As depicted in Figs. 7(b) and 7(d), the capsule positions with velocity extrema ($V_{\min}$ - - - and $V_{\max}$ - - -) and the capsule positions with area extrema are staggered. The capsule shows maximum area $\mathcal{A}_{\max}$ during the acceleration from $V_{\min}$ to $V_{\max}$, as a result of the large velocity difference on the front and back portions of the membrane. Similarly, the capsule

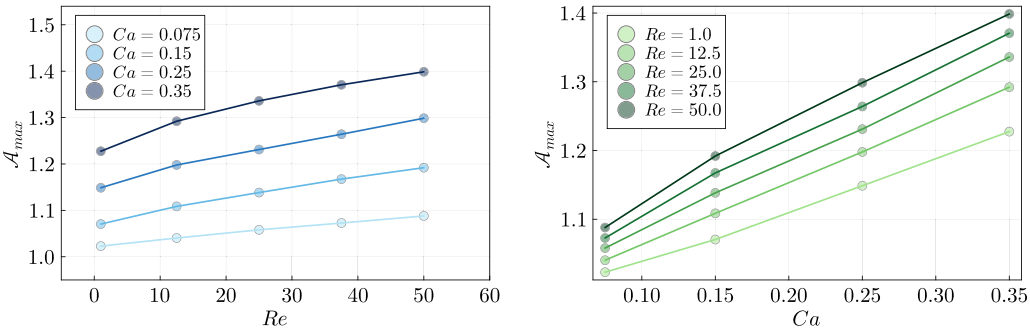

(a) $\mathcal{A}_{max}$ as a function of Re

(b) $\mathcal{A}_{max}$ as a function of Ca

FIG. 8. Maximum surface area $\mathcal{A}_{\text{max}}$ as a function of Re and Ca for a single capsule passing through the corner.

exhibits its minimal area $\mathcal{A}_{\text{min}}$ as a consequence of its deceleration, the membrane tail catching up with the membrane front. Consequently, the evolution of the capsule surface area is determined by the presence of vortices and by the velocity gradient within the flow field. These factors are, in turn, determined by the shape of the channel geometry. Additionally, Figs. 7(e) and 7(f) reveal that Re has a very strong influence on the deformation of the capsule. At a small capillary number Ca = 0.075, the ratio of maximum to equilibrium surface area $\mathcal{A}_{\text{max}}/\mathcal{A}_{\text{eq}}$ exhibits a noticeable increase from 1.02 at Re = 0.01 to 1.09 at Re = 50. In the case of a more deformable capsule, at Ca = 0.35, the increase in $\mathcal{A}_{\text{max}}/\mathcal{A}_{\text{eq}}$ is even more pronounced, rising from 1.22 at Re = 1.0 to a substantial 1.4 at Re = 50. These observations underscore the significant changes in the surface area of a capsule transitioning from non-inertial to highly inertial regimes. Surprisingly, in the stokes regime, a nonmonotonous behavior of the capsule surface area is observed from Re = 0.01 ($\mathcal{A}_{\text{max}} = 1.25$) to Re = 1 ($\mathcal{A}_{\text{max}} = 1.22$) in Fig. 7(f). In the following section, we delve deeper into the capsule deformation.

C. Maximum deformation of the capsule

The maximum surface area $\mathcal{A}_{\text{max}}$ of the capsule is presented in Fig. 8, as a function of both the Reynolds number and the Capillary number. To better analyze the trends in this figure, we also report the maximum area at intermediate Reynolds numbers, namely at Re = 12.5 and 37.5. The data reported in Fig. 8 clearly exhibits a double linear scaling of $\mathcal{A}_{\text{max}}$ with both Ca and Re as long as Ca is below 0.35—at Ca = 0.35, the shape of the curve $\mathcal{A}_{\text{max}}$(Re) is slightly concave. The slope of the scaling is about 0.003 for $\mathcal{A}_{\text{max}}$(Ca) and 1.12 for $\mathcal{A}_{\text{max}}$(Re). This means that the maximum capsule deformation responds proportionally to the Capillary number, but also to the Reynolds number. To our knowledge, this is the first time such a trend has been reported and established for low (Re = 1) to moderate (Re = 12.5, 25, 37.5, 50) inertial regimes. We believe that this result can be used as a predictive tool for many studies involving single capsules traveling through channel corners, as the maximum deformation observed for a capsule is a measure of its mechanical integrity, which is of major interest in many microfluidic applications.

Additionally, we present in Fig. 9 the maximum and minimum velocity of the single capsule flowing through the corner. In the non-inertial regime, the maximum velocity of the capsule increases with Ca, as shown in Fig. 9(a). In inertial conditions, we observe that V_{max} increases for Re ranging from 1 to 50. The increase in V_{max} between Re = 1 and Re = 50 is significant in Fig. 9(a), especially for large Ca. For instance, at Ca = 0.35, V_{max} increases by about 8% between the non-inertial and the highly inertial regimes. We then consider the evolution of the minimum velocity V_{min} for a single capsule at various Ca and Re in Fig. 9(b). In general, we observe that the minimum velocity decreases with Ca in both the non-inertial and the inertial regimes for Re $\leqslant$ 25.

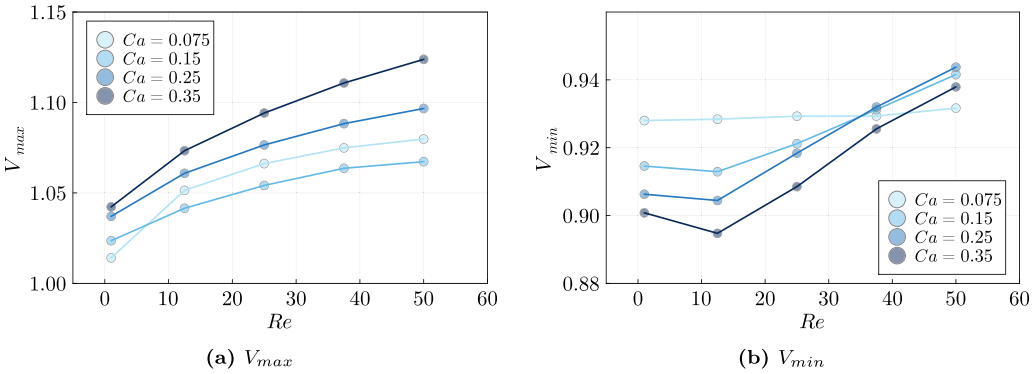

(a) V_{max} (b) V_{min}

FIG. 9. Maximum (minimum) velocity $V_{\max}$ ($V_{\min}$) as a function of Re and Ca for a single capsule passing through the corner.

In Fig. 9(b), we also observe a nonmonotonous behavior of $V_{\min}$ at low inertia and at sufficiently high Ca: for Ca $\geqslant 0.15$, $V_{\min}$ first decreases with increasing Re, reaching a minimum for Re $= 12.5$, before increasing sharply at Re > 12.5. Overall, we observe from Fig. 9 that the presence of inertia tends to increase both velocity extrema of the capsule, especially at large Ca.

A quantity of practical interest to experimentalists is the maximum stress experienced by the capsule, as it can be used to predict *a priori* if a given geometry can induce plastic deformation or even breakup of the capsule membrane [5]. More specifically, it is the largest eigenvalue $\tilde{\sigma}_2$ of the stress tensor $\tilde{\boldsymbol{\sigma}}$ that can bring insight into the mechanical integrity of the membrane. In Fig. 10, we show the maximum and average values of $\tilde{\sigma}_2$ over the membrane surface as the capsule approaches and flows through the corner at Ca $= 0.35$ and Re $= 1$, 25 and 50. We observe that $\tilde{\sigma}_{2,\,\text{avg}}$ follows a trend very similar to that of the capsule surface area observed in Fig. 7(f): $\tilde{\sigma}_{2,\,\text{avg}}$ varies smoothly with time, presents a maximum near $t = 1$ and a local minimum near $t = 2.5$, and the value of the maximum deviation from steady state nearly doubles between the low and moderate inertial cases Re $= 1$ and Re $= 50$. We also note that the steady state value of $\tilde{\sigma}_{2,\,\text{avg}}$ prior to entering the corner is

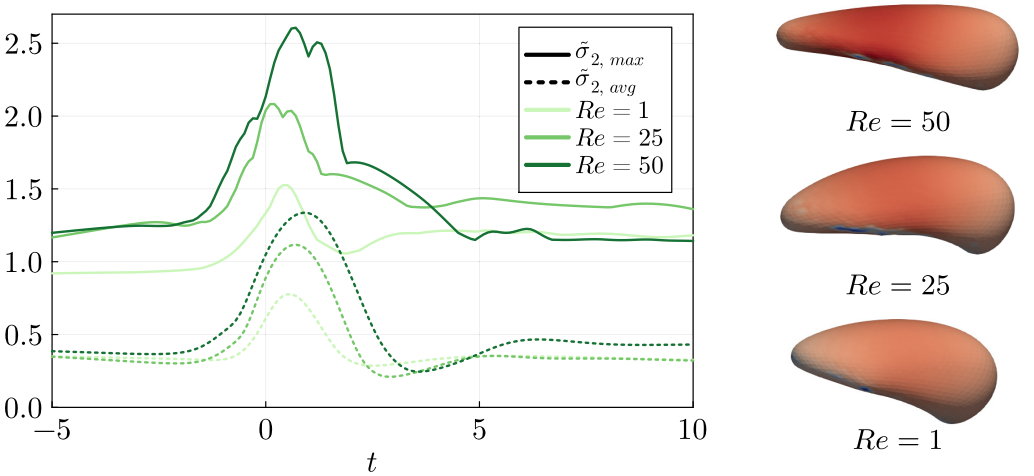

FIG. 10. Left: Maximum and average tensions in the capsule at Ca $= 0.35$ and Re $= 1$, 25 and 50. Right: Capsule shape colored by $\tilde{\sigma}_2$ when $\tilde{\sigma}_{2,\,\max}$ is reached.

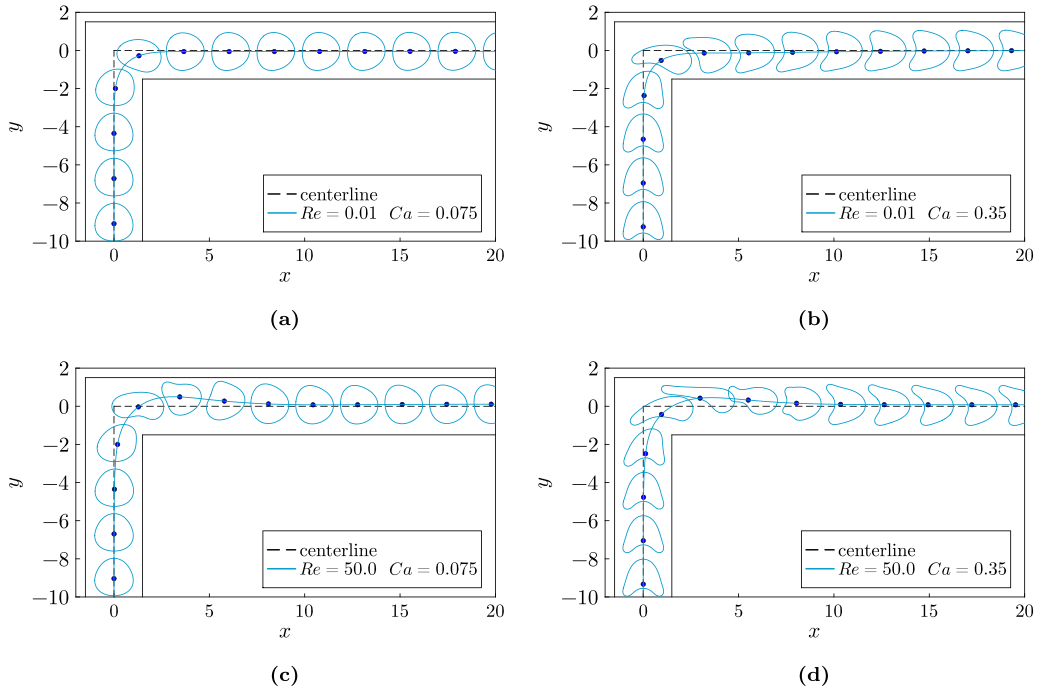

FIG. 11. Sequence of Capsule outlines for different Ca and Re. The time between each frame is $t = 1.5$.

independent of Re, as was observed in the case of the capsule surface area in Fig. 7(f). In particular, we find by comparing Figs. 7(f) and 10 that at Ca $= 0.35$, a nondimensional surface area $\mathcal{A}$ of about 1.14 leads to an average nondimensional membrane stress of about 0.4. The steady state of the maximum stress $\tilde{\sigma}_{2,\,\max}$, however, increases by about 40% between the low inertial case (Re $= 1$) and the moderate inertial cases (Re $= 25$, 50). Inside the corner, $\tilde{\sigma}_{2,\,\max}$ increases by nearly 75% between Re $= 1$ and Re $= 50$, confirming that a capsule in a moderate inertial regime has a higher risk of breakup than in a low inertial regime.

It is worth noting that for all Re, the value of the maximum stress $\tilde{\sigma}_{2,\,\max}$ is about double that of the average stress $\tilde{\sigma}_{2,\,\mathrm{avg}}$: since we showed previously that $\tilde{\sigma}_{2,\,\mathrm{avg}}$ is closely related to the capsule surface area—a quantity that is relatively easy to measure experimentally—this observation can be used by experimentalists as a rule of thumb to estimate the maximum stress in the capsule membrane and assess the mechanical integrity of the membrane.

D. Evolution of the capsule shape

We now illustrate the temporal evolution of the capsule traveling through the corner. Figure 11 shows the outline of the capsule in the symmetry plane $z = 0$ for successive discrete times. The capsule outlines are given for Ca $= 0.075$ and Ca $= 0.35$, and for Re $= 0.01$, 25, and 50. Prior to entering the corner, the capsule adopts a steady shape that is determined by the confinement of the walls. In the case of Ca $= 0.35$, we observe the well-known "parachute" shape. Upstream of the corner, the trajectory of the capsule coincides with the centerline of the primary (vertical) channel. As the capsule flows through the corner, the capsule deviates from the channel centerline: in the non-inertial regime, Zhu and Brandt [38] showed that the capsule trajectory closely matches the flow streamlines. We obtain the same conclusion in the inertial regime. When inertia is considered, the capsule trajectory crosses the horizontal centerline of the secondary channel and comes increasingly close to the upper wall as Re increases, before relaxing to the channel centerline.

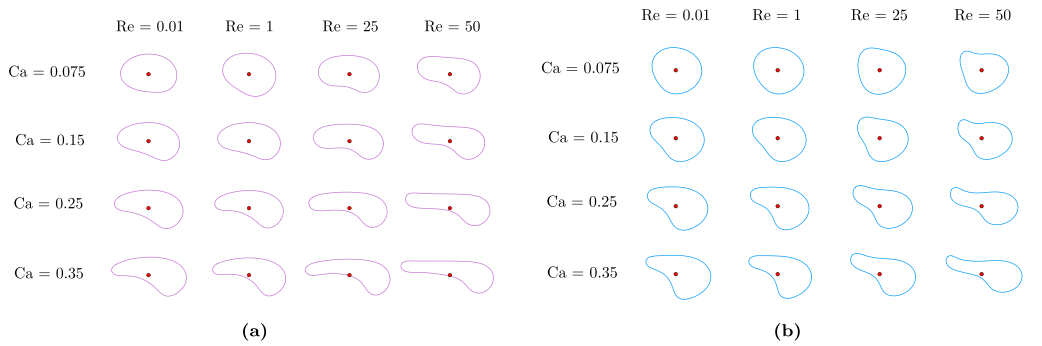

FIG. 12. Outlines of a single capsule passing a corner with (a) maximum surface area $\mathcal{A}$ and (b) maximum velocity V at various Re and Ca.

Figures 11(a) and 11(b) show clear differences in the effects of Ca in the Stokes regime. Increasing Ca from 0.075 to 0.35 causes the equilibrium shape of the capsule to change from an slightly deformed spheroid to a concave "parachute" shape. For a small Ca = 0.075, the equilibrium shapes of the capsule remain similar as Re increases from Re = 0.01 to Re = 50 [see Fig. 11(a) and 11(c)]. However, the deformation of the capsule becomes more evident inside the corner at higher Re, particularly in Fig. 11(c). After passing the corner, the capsule shape returns to its steady spheroid shape observed in the Stokes regime for all values of Re. In the case of a high Ca = 0.35, we observe that the equilibrium shape of the capsule is more and more concave as Re increases. Inside the corner, the capsule is highly elongated and presents an increasingly long tail for increasing Re—e.g., Fig. 11(d) in the case of Re = 50. In the highly inertial regime, strong lubrication interactions occur between the capsule and the top wall, resulting in a flat top surface.

In Figs. 12(a) and 12(b), we present the single capsule outline with the maximum surface area $\mathcal{A}_{\max}$ and the maximum velocity $V_{\max}$ inside the corner for all the cases investigated in this section. Inside the corner, the maximum surface area of the single capsule is reached when it approaches the upper wall and it is quickly followed by the maximum velocity. From Figs. 12(a) and 12(b), we observe in particular that a high Re leads to an elongation of the capsule in the streamwise direction, while a high Ca increases the concavity of the capsule. Moreover, we note that the centroid of the capsule moves closer to the rim of the outline at high values of Ca: note that the centroid drawn in figures Figs. 11–12(b) corresponds to the centroid of the three-dimensional capsule, not to that of the two-dimensional outline. The results shown in Figs. 11–12(b) indicate that Ca has a significant effect on capsule deformation, while Re has a more pronounced effect on the trajectory of the capsule as well as its deformation resulting from the lubrication layer against the top wall of the corner. In particular, at high Re, the capsule undergoes significant stretching, which may cause damage or even rupture in microfluidic devices. Understanding the effects of Re on capsule deformation and the resulting damage is crucial in designing efficient and reliable microfluidic devices.

E. Discussion on the Stokes regime

We observe in Fig. 7(f) a surprising, nonmonotonous behavior of the capsule surface area around Re = 1: at large Ca, the surface area of the capsule is lower at Re = 1 than at Re = 0.01 and Re = 25. Additionally, in Fig. 7(e) the steady surface area of the capsule at Re = 0.01 and Ca = 0.075 downstream of the corner is about 1% lower than the initial spherical surface area of the capsule, indicating a small loss of the internal capsule volume. The cause of these observations may be related to the limitations of the FTM coupled with a sub-optimal choice of numerical parameters in the case of Re = 0.01 only. Indeed, the immersed boundary method is known to conserve volume asymptotically rather than to machine precision. In earlier IBM studies involving capsules, the volume loss is always small, typically below 1% [8–10,23]. Moreover, Stokes conditions are known

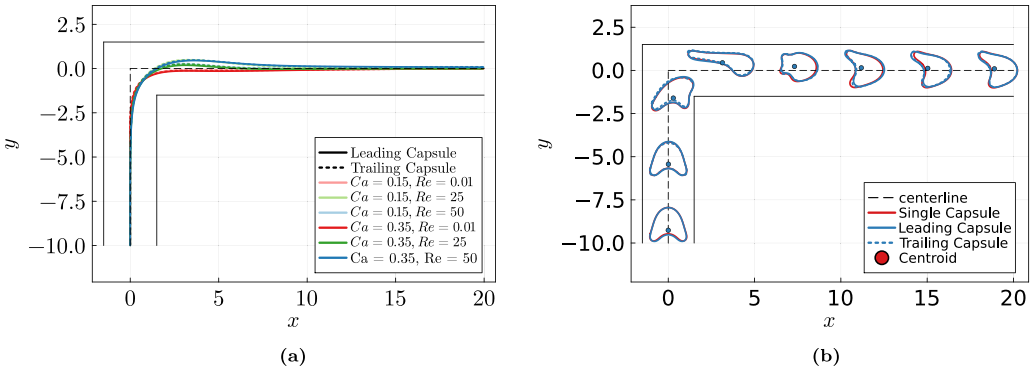

FIG. 13. (a) Trajectory of the two capsules at different Ca and Re. (b) Outlines of the leading and trailing capsules at Ca = 0.35, Re = 50, $d_0 = 0.25$, with comparison to a single capsule.

to be challenging for PDE-based incompressible Navier-Stokes solvers, as the matrix inverted in the velocity viscous Poisson problem is less well conditioned at low Re. While it is worth noting that the capsule surface area in the Stokes regime should be interpreted with caution, these limitations only affect the capsule surface area and not the centroid velocity. Moreover, our solver was extensively validated in Stokes conditions in [45] and showed excellent agreement with the BIM as well as other FTM solvers. As such, while further investigation should be conducted in the Stokes regime, it cannot be excluded that at high Ca the capsule surface area at Re = 0.01 is physically slightly greater than that at Re = 1. Finally, the main focus of the present work is to investigate the inertial motion and deformation of capsules through a sharp corner, i.e., in conditions where our FTM solver does not suffer from the limitations outlined above.

V. SYSTEM OF TWO CAPSULES

In this section, we consider two identical capsules flowing through the corner as we vary the normalized interspacing distance $d = \tilde{d}/2\tilde{a} - 1$ between the capsules as well as the Reynolds and Capillary numbers. Lu *et al.* [10] previously considered the binary interaction of capsules flowing through a T junction: they showed that when $d_0 \geqslant 1.3$ the trailing capsule has minimal impact on the motion of the leading capsule. By contrast, in their T-junction geometry, Lu *et al.* observed that the motion of the trailing capsule is significantly affected by the presence of the leading capsule. To gain insight into the physical features relevant to capsule interactions through a corner in the inertial and non-inertial regimes, we select small values for the normalized interspacing distance $d_0 = 1, 1/2$, and $1/4$ and we examine phenomena such as migration, dynamics and deformation of the leading and the trailing capsules.

A. Qualitative analysis: Trajectory and capsule shape

We first analyze the trajectory and the qualitative shapes of the pair of capsules as they flow through the corner. Figure 13(a) shows the trajectory of the capsules at Re = 0.01, 25, and 50 and Ca = 0.15 and 0.35. We note that all curves corresponding to the same Ca overlap: Ca has no impact on the path of either the leading or the trailing capsule. Likewise, we observe no significant difference in the trajectories of the leading and the trailing capsules, unlike the strikingly different paths reported in the case of a T junction [10]. In fact, the key parameter that controls the capsule trajectory is the Reynolds number. As Re increases, the inertia drives the capsule closer to the upper channel wall, as observed in Sec. IV in the case of a single capsule. We then illustrate the capsule shape on the symmetry plane $z = 0$ in Fig. 13(b) for the most deformed capsule configuration corresponding to Ca = 0.35 and Re = 50 with an initial interspacing distance $d_0 = 0.25$. We

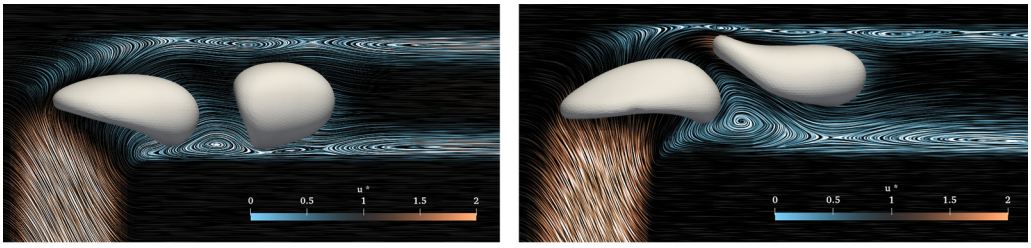

(a) (b)

FIG. 14. Streamlines and vortex structures of the perturbed flow with two capsules past a channel corner with a square cross-section (a) Re = 0.01, Ca = 0.35, $d_0 = 0.5$; (b) Re = 50, Ca = 0.35, $d_0 = 0.5$.

compare the outlines of the leading and the trailing capsules to those of a single capsule in the same conditions. Qualitatively, the deformation of interacting capsules is not significantly different than that observed in the case of a single capsule. Perhaps more surprisingly, the qualitative outlines of the leading and the trailing capsules are also very similar, almost overlapped, even in the strongly interacting configuration corresponding to $d_0 = 0.25$. Note that this qualitative shape analysis relies on the outline of the capsule in the plane of symmetry $z = 0$, while the actual three-dimensional shape of the leading and trailing capsules may differ more strongly.

To provide a clearer illustration of the two-capsule system, we present their interaction in the vicinity of a channel corner, together with the vortex structure of the flow field, as depicted in Fig. 14. We consider the most deformable capsules at Ca = 0.35 in the Stokes regime Re = 0.01, shown in Fig. 14(a), and in the inertial regime at Re = 50 in Fig. 14(b). In the secondary channel, the streamwise flow velocity along the x axis significantly exceeds the magnitudes of the transverse and the spanwise components. As such, to better highlight the flow dynamics, we subtract the mean inlet velocity and present the streamlines of the perturbed velocity field $u^* = u - U_0$ in the plane $z = 0$. In Fig. 14(a), we observe that the leading capsule undergoes deceleration while exiting the corner. In contrast, the trailing capsule is in a phase of acceleration and elongation. The substantial distance between the two capsules results in a weak interaction at Re = 0.01. With the increase of Re, the increased strength of the vortices becomes evident, as depicted in Fig. 14(b). Notably, the vortex located on the bottom wall of the secondary channel is significantly larger at Re = 50 compared to its size at Re = 0.01. In the captured snapshot, the leading capsule leaves a trail along the top of the channel, which may hinder the motion of the trailing capsule.

B. Quantitative analysis: Velocity and membrane surface area

We now compare the temporal evolution of the velocity of the centroids of the capsules as well as the time evolution of their surface areas, as plotted in Fig. 15. To simplify the identification of interaction features, we first focus on the most deformed configuration corresponding to Ca = 0.35, Re = 50, and $d_0 = 0.25$. For reference, we also plot the evolution of a single capsule under the same conditions in red. Throughout the remainder of this study, and unless otherwise stated, the velocity of interacting capsules is normalized by the equilibrium velocity V_{eq} of a single capsule for the same Capillary and Reynolds numbers. This normalization choice allows for an unbiased comparison between the velocities of the leading and the trailing capsules. In this section we also denote the reduced velocity of the single capsule by V_s, that of the leading capsule by V_l, and that of the trailing capsule by V_t. Similarly, we denote by $\mathcal{A}_s$, $\mathcal{A}_l$, $\mathcal{A}_t$ the normalized surface areas of respectively the single, leading and trailing capsules.

In Fig. 15(a), we observe that the velocity of the leading capsule is affected by the presence of the trailing capsule before it reaches the corner, as it is about 1% higher than that of a single

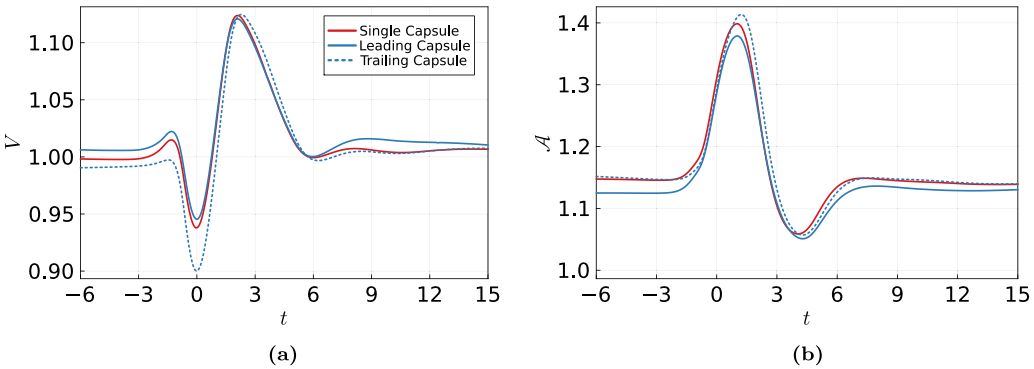

FIG. 15. Temporal evolution of the velocity V and the surface area $\mathcal{A}$ of capsules at Ca = 0.35, Re = 50 with $d_0 = 0.25$: a comparison of the leading, trailing and a single capsules.

capsule. However, the extrema of V_l as it flows through the corner closely match those of V_s. After the corner, V_l is about 2% larger than V_s but slowly relaxes back to V_s further downstream. Concerning the trailing capsule, we note that its velocity is more markedly affected by the presence of the leading capsule. Before reaching the corner, V_t is about 1% lower than V_s, but inside the corner, its minimum value is 4% lower than V_s. However, the maximum of V_t is identical to that of both V_l and V_s. Downstream of the corner, V_t quickly relaxes back to V_s and maintains a similar value thereafter, eventually converging to V_{eq}. The interaction between the two capsules is clearly visible in Fig. 15(a). Initially separated by a distance of $d_0 = 0.25$, the fluid situated between the capsules functions akin to a weak spring. This dynamic causes the leading capsule to accelerate slightly, achieving a marginally higher velocity, while simultaneously exerting a restraining force on the trailing capsule, resulting in a slightly reduced velocity. In VC, we will demonstrate that the relaxation period of this spring-like layer of fluid is notably extended. This prolonged relaxation directly contributes to a persistent discrepancy in velocity between the leading and trailing capsules, observable both before and after they pass the corner. The low V_{min} of the trailing capsule in Fig. 15(a) results from two primary factors: the blockage of the interior sharp corner and also the hindrance due to the tail of the leading capsule as illustrated in Fig. 14(b). The time evolution of the surface areas of the pair of capsules is shown in Fig. 15(b). The normalized surface area of the leading capsule $\mathcal{A}_l$ is clearly influenced by the presence of the trailing capsule, as was observed above in the case of its velocity. The steady and maximum surface areas of the leading capsule are about 2% lower than that of the single capsule. In contrast, the steady surface area of the trailing capsule closely matches that of the single capsule upstream and downstream of the corner, while its maximum value is about 1% higher than that of the single capsule. We hypothesize that the small interspacing distance between the two capsules disturbs the wake behind the leading capsule, which tends to mitigate its deformation on the concave rear surface and therefore decreases its surface area. Conversely, as the wake of the trailing capsule is unaffected, the discrepancies between its surface area and that of the single capsule are less pronounced.

We then present the time evolution of the velocity and surface area of the leading and the trailing capsules at various Ca, Re, and d_0. We first focus on the velocity of the capsules, displayed in Fig. 16(a) for Ca = 0.15 and 0.35 and for $d_0 = 0.5$ and 1. The velocity of both capsules displays a minimum at $t = 0$ and a maximum at $t \approx 2$ at Ca = 0.15 and Ca = 0.35. The extrema of the velocity are more pronounced as Ca increases. The effects of the initial interspacing distance d_0 on these extrema are less evident but still present: the velocity maxima of both the leading and the trailing capsules are increased by about 1% as d_0 is halved from 1 to 0.5. Interestingly, the relaxation time of V_t to V_{eq} is significantly reduced when compared to that of V_l: about 4 time units

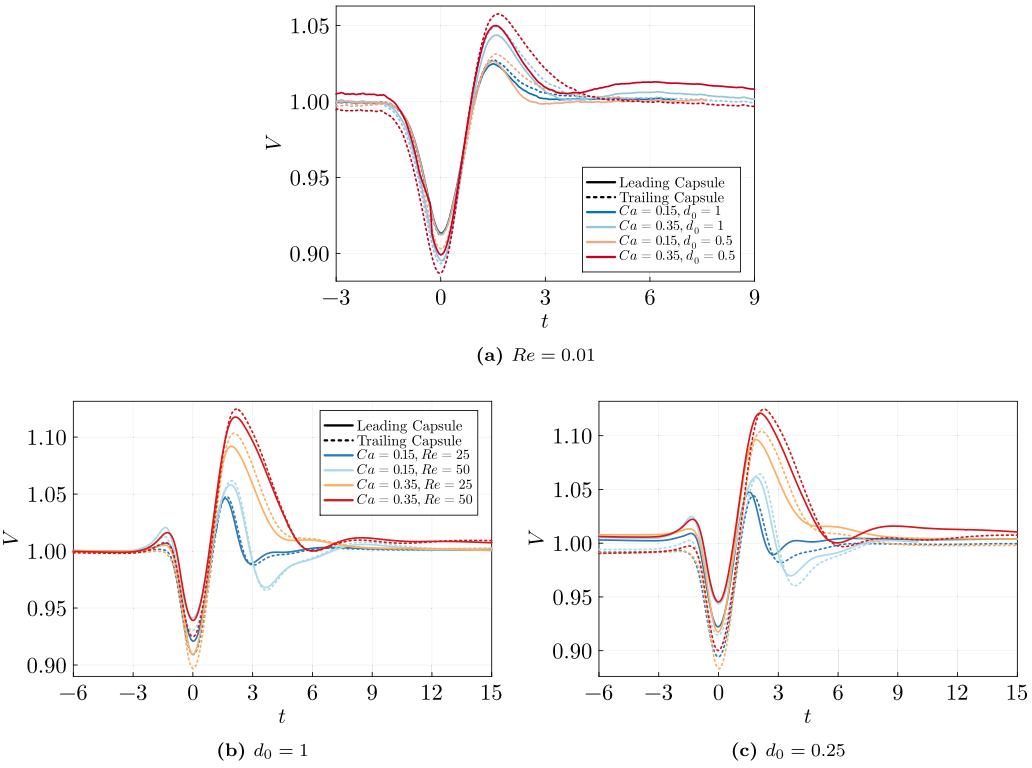

(a) $Re = 0.01$

(b) $d_0 = 1$

(c) $d_0 = 0.25$

FIG. 16. Temporal evolution of V of the leading and trailing capsules at different Ca, Re, and d_0.

in the case of V_t with respect to more than 10 time units in the case of V_l. Capsule velocities in the inertial regimes at Re = 25 and 50 and at Ca = 0.15 and Ca = 0.35 are plotted in Figs. 16(b) and 16(c) for $d_0 = 1$ and 0.25, respectively. The results are similar to that of the non-inertial regime: Ca enhances the velocity deviations and the extrema are more pronounced in the case of the trailing capsule. Surprisingly, we note that Figs. 16(b) and 16(c) are almost identical: we conclude that the interspacing distance does not to impact the capsule maximum velocities inside the corner. A plausible explanation is that the capsule acceleration is predominantly determined by the strength of the Dean vortices. In comparison, the effects of the capsule deformation and interaction on the fluid motion are of minor importance. With the same Re and Ca, the acceleration process is similar for the capsule pair with different initial distances leading to the similar $V_{\max}$ values. As discussed in Fig. 15(a), the short interspacing creates a layer of fluid analogous to a spring between the capsule pair and leads to a faster leading and a slower trailing capsule upstream and downstream from the corner. Within the corner, the interplay between the capsules [as shown in Fig. 14(b)] can lead to a larger difference on $V_{\min}$ in Figs. 16(b) and 16(c). More discussions about the interspacing of the capsule pair are provided in Sec. V C.

When analyzing the capsule surface areas for varying Re, Ca and d_0, a similar behavior is found: the surface area of the trailing capsule is consistently greater than that of the leading capsule, and increasing Capillary and Reynolds numbers and decreasing the initial interspacing distance enhance this phenomenon. In particular we report in Table I the maximum surface areas of the leading capsule and in Table II that of the trailing capsule. As can be seen from Tables I and II, the maximum surface area of the leading capsule exceeds that of the trailing capsule by up to 5%. The full time-dependant data is provided in Appendix A.

TABLE I. Maximum surface area $\mathcal{A}_{max}$ of the leading capsule at different Ca, Re, and d_0.

d_0		Re = 0.01	Re = 25	Re = 50
1	Ca = 0.15	1.065	1.138	1.193
	Ca = 0.35	1.263	1.334	1.399
0.5	Ca = 0.15	1.065	1.135	1.186
	Ca = 0.35	1.247	1.323	1.383
0.25	Ca = 0.15	1.068	1.129	1.180
	Ca = 0.35	1.236	1.308	1.379

C. Time evolution of the interspacing distance

We now analyze the time evolution of the interspacing distance between the two confined capsules considered in this section. Figure 17 shows the time-dependent interspacing distance for Ca = 0.15 and 0.35, Re = 25 and 50, and $d_0 = 1$, 0.5, and 0.25. In this figure, we note that in all cases, the interspacing distance decrease immediately after the trailing capsule is released. This is due to the fact that upon release, the trailing capsule is spherical and therefore located farther away from the channel walls than is the leading capsule, resulting in its initial acceleration before a steady shape is found - typically within less than five time units. In the case of $d_0 = 1$, the time-dependent interspacing distance d is steady until the leading capsule approaches the corner, then reaches a minimum and a maximum inside the corner and becomes steady again as the trailing capsule leaves the corner region. Interestingly, the steady interspacing distance downstream of the corner is up to 10% greater than its steady value prior to the corner, suggesting that the corner separates the two capsules. Moreover, the initial interspacing distance is greater in the case Re = 25 than in the case Re = 50: this is only an artifact of our release mechanism. Indeed, the steady "parachute" shape of the capsule is deployed faster at Re = 50 than at Re = 25, leading to a shorter initial acceleration phase of the trailing capsule towards the leading capsule at Re = 50 than at Re = 25. When $d_0 = 0.5$ and $d_0 = 0.25$, we observe that the interspacing distance steadily increases until the capsules reach the corner region where it displays the same behavior as in the case of $d_0 = 1$, and continues to increase downstream of the corner. While a steady value of d is not clearly reached within the considered time range, we can extrapolate the trend and conclude that the interspacing distance seems to saturate to values ranging from 0.6 to 0.8 depending on Re, Ca, and d_0. Therefore, the pair of confined capsules we consider exhibit a minimum stable interspacing distance d_{min}. Moreover, we note that the slope of d is greater in the case of lower initial interspacing distances, showing that the relative velocity of the capsules is a function of their interspacing distance.

TABLE II. Maximum surface area $\mathcal{A}_{max}$ of the trailing capsule at different Ca, Re and d_0.

d_0		Re = 0.01	Re = 25	Re = 50
1	Ca = 0.15	1.068	1.143	1.201
	Ca = 0.35	1.271	1.342	1.417
0.5	Ca = 0.15	1.070	1.144	1.204
	Ca = 0.35	1.277	1.345	1.414
0.25	Ca = 0.15	1.069	1.148	1.204
	Ca = 0.35	1.277	1.344	1.41

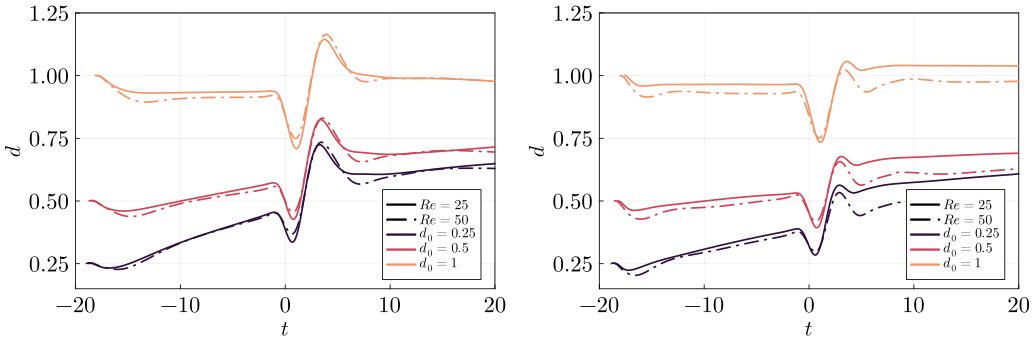

(a) $Ca = 0.15$ (b) $Ca = 0.35$

FIG. 17. Temporal evolution of d for different initial interspacing distance d_0 and Reynolds number Re.

The present analysis of the binary interaction of capsules through a corner reveals that the two considered capsules do interact in this geometry, affecting their motion and deformation. In particular, the trailing capsule tends to be more deformed than the leading capsule, and the corner tends to separate the pair of capsules. A natural question that arises is that of the accumulation of such effects if more than two capsules are considered.

VI. TRAIN OF TEN CAPSULES

In this last section, we investigate the behavior of a train of ten capsules flowing through the corner. We insert each capsule using the same procedure employed in the previous section: a new initially spherical capsule appears at a distance $D_c = 30$ radii from the corner as soon as the preceding capsule has advanced by a distance $\tilde{d} = 2\tilde{a}(1 + d_0)$. The capsules are removed from the computational domain when they are less than one initial diameter away from the outflow boundary. Our goal is to determine if the findings of the previous binary capsule analysis accumulate when more than two capsules are considered, especially with regard to the increased surface area of the capsules and the separating effect reported in Sec. V. As such, we plot in Fig. 18 the normalized surface area and velocity of each capsule of the train at Re = 50, $d_0 = 0.125$ and Ca ranging from 0.15 to 0.35. The same figure obtained in the case of $d_0 = 1$ is provided in Appendix B. In this section, we define the time origin as the time instant the first capsule reaches its lowest velocity ($t_{1,\min}$). This approach allows for a clear depiction of the temporal progression of each capsule as it flows through the corner. In the same manner as in the previous section, the velocity of the capsules within the train is normalized by the equilibrium velocity V_{eq} of the single capsule experiencing the same Ca and Re. In Fig. 18, the darkness of the color corresponds to the position of the capsule in the train: darker means increasing capsule number, i.e., further downstream along the capsule train. As mentioned in Sec. V, the initial peaks in the surface area and velocity of the capsule are insertion artifacts and do not contribute to the physics that is the focus of this section. We observe in Fig. 18 that the behavior of the last capsule is significantly different than that of the rest of the train. In Sec. V we hypothesized that the difference in surface areas of the leading and the trailing capsules is since the wake of the leading capsule is significantly affected by the presence of the trailing capsule. The present observation in Fig. 18 corroborates this statement: All of the capsules in the train see their wake affected by a trailing capsule, except in the case of the last capsule. As discussed previously, the interaction between two successive capsules can effectively reduce the $V_{\min}$ of the trailing capsule, as depicted in Fig. 16(c). This effect accumulates as the number of capsules increases in the train in Fig. 18. When only two capsules are considered, we saw that they exhibit similar $V_{\max}$ values. However, when a train of capsules is considered, the

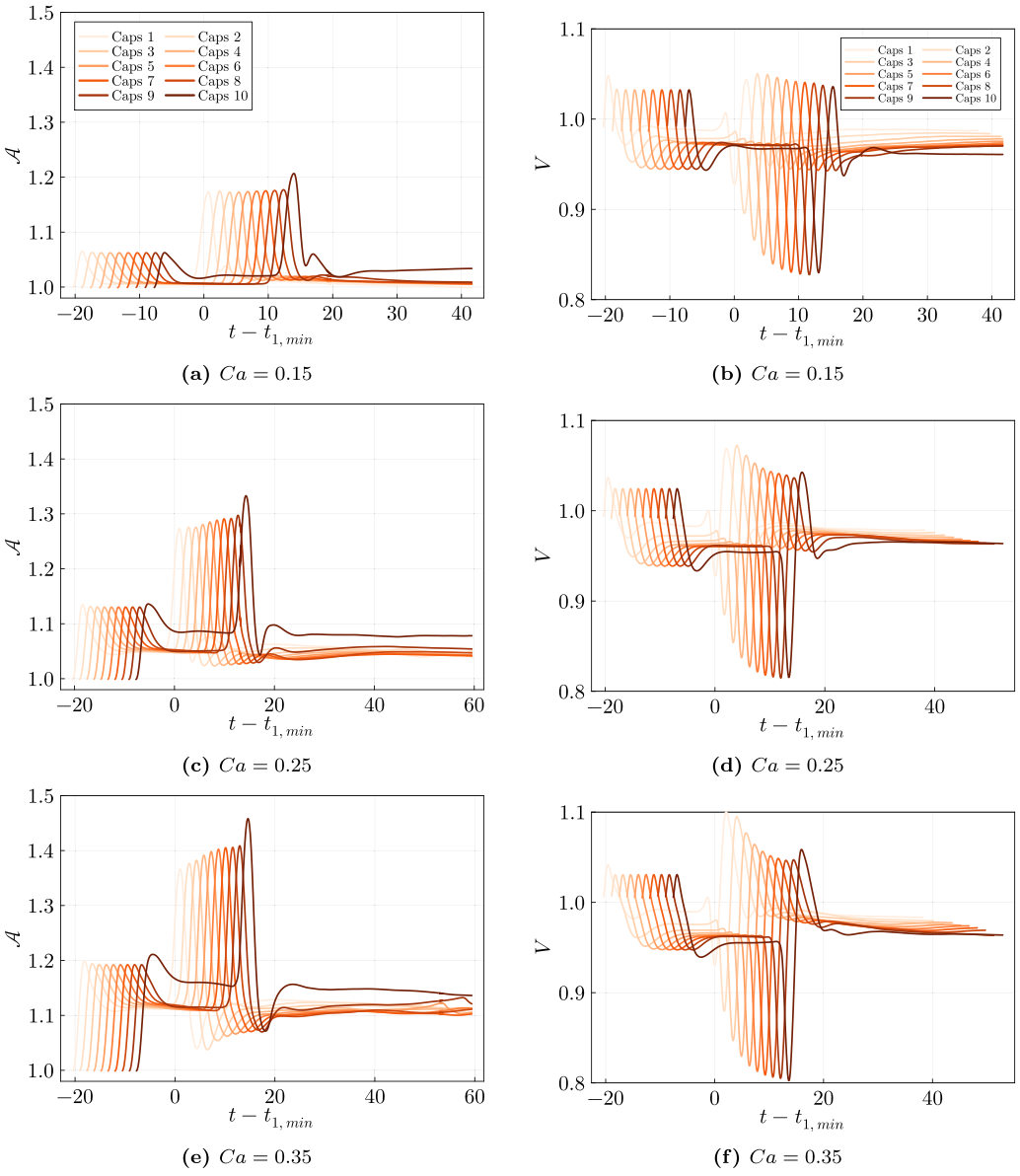

(a) $Ca = 0.15$ **(b)** $Ca = 0.15$

(c) $Ca = 0.25$ **(d)** $Ca = 0.25$

(e) $Ca = 0.35$ **(f)** $Ca = 0.35$

FIG. 18. Time evolution of the reduced surface areas and velocities of a train of ten capsules at Re = 50 and $d_0 = 0.125$ for Ca = 0.15, 0.25, and 0.35.

Dean vortices are continuously affected by the flow of capsules and we observe a decrease in $V_{\max}$ in Fig. 18. As the last capsule flows through the corner, $V_{\max}$ rises within the corner in a similar fashion as the first capsule of the train. As noted in Figs. 7(b) and 7(d), the maximum area of the capsule flowing through a corner is reached during the acceleration phase. With a small $V_{\min}$ and a relatively high $V_{\max}$, the last capsule exhibits an exceptionally high $\mathcal{A}_{\max}$. We also remark in Fig. 18 that this effect is enhanced with increasing Ca. While noteworthy in the case of a pair of capsules, the behavior specific to the last capsule is less pertinent to the study of a train of capsules, as only the

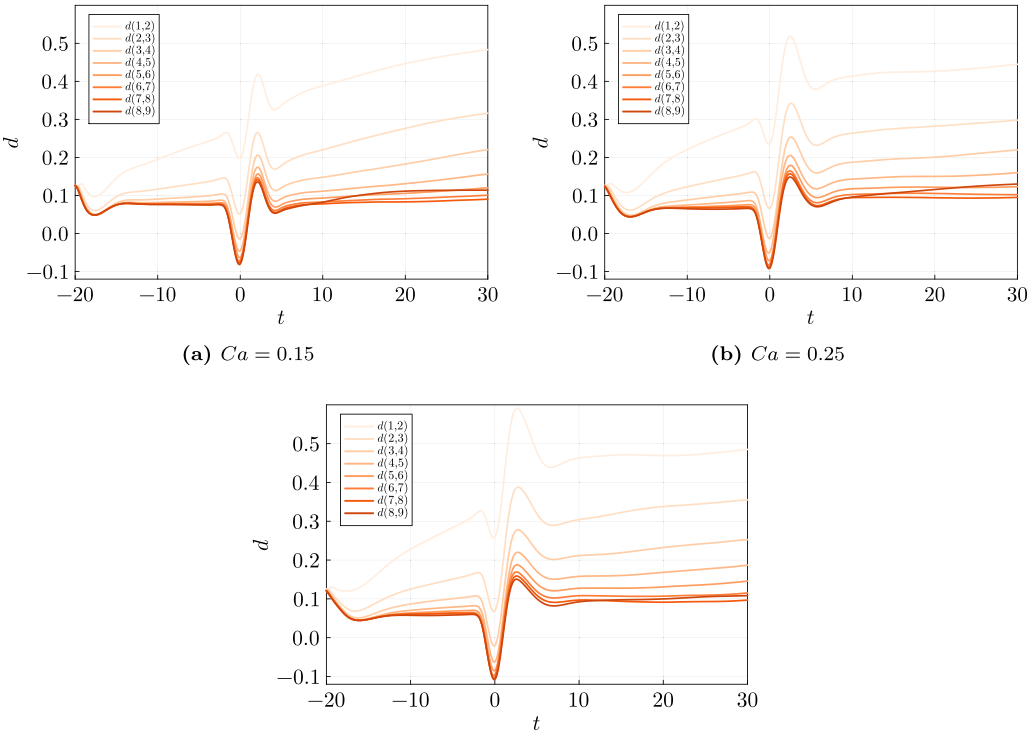

(a) $Ca = 0.15$ **(b)** $Ca = 0.25$

(c) $Ca = 0.35$

FIG. 19. Temporal evolution of d for a train of 10 capsules at Re $= 50$ and $d_0 = 0.125$ for (a) Ca $= 0.15$, (b) Ca $= 0.25$, and (c) Ca $= 0.35$.

core of the capsule train is relevant to typical microfluidic applications. As such, in the remainder of this section, our analysis is focused on the first nine capsules of the train.

As expected, we confirm in Fig. 18 that a steady state is reached in the straight channel prior to the corner for each capsule and for all Ca. While the steady surface area remains constant with increasing capsule number, i.e., as we move further downstream along the train of capsules, we observe that the velocity of the capsules decreases. In particular, the difference between the steady velocity of the first and ninth capsules increases with increasing Ca. As the capsules enter the corner region, they display the familiar pattern previously described in Secs. IV and V, before relaxing to steady values. The shape of the deviation pattern is strikingly similar across different capsules of the train, regarding both the velocity and the surface area of the capsules, except that they are shifted in time and magnitude. More precisely, the surface area curves are shifted upwards with increasing capsule number while the velocity curves are shifted downwards with increasing capsule number. As a result, the maximum surface area of the capsule increases and the velocity extrema decreases with increasing capsule number. This behavior is more pronounced as Ca increases. Additionally, we compare in Fig. 19 the normalized interspacing distance d between each pair of capsules in the train. In Fig. 19, each curve is shifted in time such that $t = 0$ corresponds to $d(t = 0) = d_{\min}$ inside the corner. For all Ca, we observe that the interspacing distance $d(1, 2)$ between the first and the second capsules increases to a steady value close to 0.5, and that the corner has marginal effects on the downstream evolution of $d(1, 2)$: this behavior is identical to the case of two capsules studied in the previous section. However, as we move downstream along the train of capsules, d increases

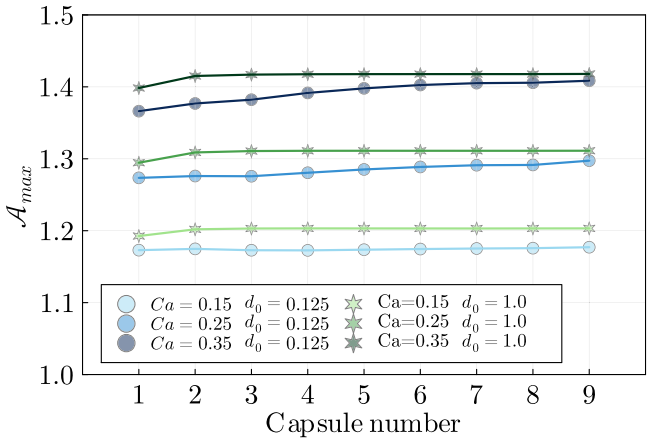

FIG. 20. $\mathcal{A}_{\max}$ as a function of the capsule number.

slower and slower prior to the corner until it remains constant for capsule numbers greater than 7, at a steady value $d \approx 0.07$ that decreases only marginally with increasing Ca. After the transient regime due to the corner, $d(i, i+1)$ for capsule numbers i greater than 7 reaches a steady state that is slightly higher than before entering the corner. In other words, the corner tends to increase the interspacing distance and therefore exhibits a separating effect. This separating effect is observed regardless of the initial interspacing distance d_0, as was the case in the previous section when only two capsules were considered.

Finally, to investigate further the influence of the capsule number on the capsule dynamics, we plot in Figs. 20 and 21 the maximum surface area as well as the maximum and minimum velocities of each capsule of the train for varying Capillary numbers and interspacing distances. Again, the $V_{\max}$ and $V_{\min}$ are normalized by the equilibrium velocity V_{eq} of the single capsule at the same Re and Ca. The difference in minimum velocity (respectively, maximum velocity) between the first and the ninth capsule is about 14% (respectively, about 5%) at $\text{Ca} = 0.35$ while it is about 11% (respectively, 2%) at $\text{Ca} = 0.15$. Similarly, the difference in maximum surface area between the first and the ninth capsule is about 4% at $\text{Ca} = 0.35$ and less than 1% at $\text{Ca} = 0.15$.

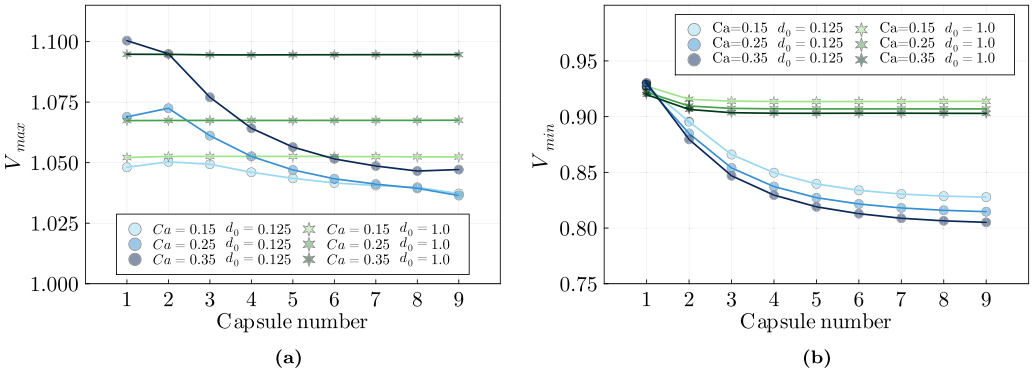

FIG. 21. (a) $V_{\max}$ and (b) $V_{\min}$ as a function of the capsule number.

These results correspond to $d_0 = 0.125$, while in the case of $d_0 = 1$ only deviations lower than 1% are observed in the extrema of the capsule surface area and velocity (except in the case of $V_{\min}$ for which velocity deviations of 2% are observed). The very small deviations observed in the case $d_0 = 1$ indicate that for this interspacing distance, the capsules interact very weakly. As such, there exists a critical interspacing distance d_c below which capsule interactions are observed, with $0.125 < d_c < 1$.

The fact that d_c is less than 1 can be surprising, as a normalized interspacing distance of $d_0 = 1$ would typically be classified as a strongly interacting regime in other geometries, e.g., in the T junction investigated by Lu *et al.* [10]. The main reason for the low interaction we observed is likely due to the short residence time of the capsules in the corner region. Indeed, Lu *et al.* showed that the residence time is determinant in the path selected by the capsules in a T junction geometry. Another reason for such a low critical interspacing distance is related to the very confined configuration we study: the capsule shape and behavior is primarily due to the presence of the walls, while the small disturbances of the flow field due to the other capsules only marginally contribute to each capsule dynamics. Future studies could explore the dynamics of a train of capsules in a wider channel, i.e., in a less confined configuration, where each capsule could be more influenced by the wake disturbances of their preceding neighbor.

VII. CONCLUSION

In the present work, the inertial and non-inertial dynamics of three-dimensional elastic capsules flowing through a sharp corner are investigated. The capsule trajectory, surface area, velocity and membrane stress are analyzed in the cases of one, two and a train of ten capsules released upstream of the corner. The channel Reynolds number ranges from 0.01 to 50, the Capillary number representing the ratio of viscous stresses over elastic stresses ranges from 0.075 to 0.35 and the initial normalized interspacing distance between two capsules is varied from 0.125 to 1. The goal of this study is to help provide practical guidelines to anticipate capsule breakup and estimate throughput in inertial microchannels.

The case of a single capsule with no inertia was previously studied by Zhu and Brandt [38], who reported that the capsule follows the flow streamlines closely regardless of the Capillary number. In inertial flows, we found that this statement is still valid for all considered Reynolds and Capillary numbers. As the streamlines of the inertial flow cross the centerline of the secondary channel—the horizontal channel downstream of the corner—the capsule position is increasingly close to the top wall for increasing Reynolds number, especially in the case of large Capillary numbers. However no collision between the capsule and the wall of the secondary channel was observed thanks to strong lubrication forces. In their study, Zhu and Brandt also analyzed the velocity of the capsule centroid and the surface area of the capsule membrane: they found that the capsule velocity decreases in the corner and increases immediately after the corner, with an overshoot increasing with membrane deformability. The surface area of the capsule was also found to reach a maximum slightly shifted in time with respect to the minimum of velocity. In the inertial regime, we observed that this behavior is enhanced as the Reynolds number increases. However our results at $\mathrm{Re} = 1$ do not differ significantly from results obtained in the non-inertial regime, which corroborates the same observation made by Wang *et al.* [8,9]. Moreover, at sufficiently high inertia, capsule surface areas lower to equilibrium surface areas are observed as the capsule relaxes to its steady state. In other words, immediately after the corner the capsule oscillates around its steady shape. This phenomenon is enhanced as the Capillary number increases. Additionally, we reported that the relationship between the maximum surface area $\mathcal{A}_{\max}$ of the capsule and the Reynolds number is linear as long as the Capillary number is kept below 0.35. At $\mathrm{Ca} = 0.35$, the relationship between $\mathcal{A}_{\max}$ and Re is not perfectly linear and the curve $\mathcal{A}_{\max}(\mathrm{Re})$ is slightly concave. Moreover, from $\mathrm{Re} = 1$ to $\mathrm{Re} = 50$, the maximum surface area increases nearly linearly over the full range of Ca. At $\mathrm{Ca} = 0.35$, we compared the membrane stress to the capsule surface area and found that (i) the time evolution of the average stress presents a strong correlation to that of the membrane

surface area, and (ii) in our configuration, the value of the maximum stress is double that of the average stress. As a result, observing the capsule surface area experimentally can provide reliable insight into the average stress as well as an estimate of the capsule maximum stress. This finding is of primary importance in the design of microfluidic devices where capsule breakup is to be avoided, as well as in the development of targeted drug delivery methods for which a controlled capsule breakup is sought.

We then investigated the interaction of several capsules in the corner geometry. First, two capsules are considered with varying initial interspacing distances. Similar to the case of a single capsule, neither the trajectory of the leading nor of the trailing capsules is observed to significantly deviate from the flow streamlines. In the considered range of initial interspacing distances, the velocity of the trailing capsule is found to be generally lower than that of the leading capsule as well as that of a single capsule at the same Reynolds and Capillary numbers. Similarly, the velocity of the leading capsule is greater than that of a single capsule in the same conditions. This velocity difference is also visible in the time evolution of the interspacing distance d between the pair of capsules. In particular, we found that capsules initially located at $d_0 \leqslant 0.5$ tend to separate. This suggests that there exists a minimum stable gap $d_{\min} > 0.5$ between two confined capsules. A systematic analysis of this effect is left for future studies. In contrast, inside the corner the surface area of the trailing capsule is found to be larger than that of the leading capsule and of the single capsule in the same conditions. However, in the configuration we consider where confinement is strong, the magnitude of these effects is small even for capsules located very close to each other: the velocity of the leading and trailing capsules only deviates by a few percents from that of a single capsule. Next, we examined the case of a train of capsules and sought to determine whether the effects observed with a pair of capsule accumulate. While no interaction occurs for a large initial interspacing distance $d_0 = 1$, we found that in the case $d_0 = 1/8$, the steady and extremum surface areas of the trailing capsules increase by up to 5% and eventually saturate at the tail of the train, around the ninth capsule. In all cases for which $d < d_{\min}$, the corner is found to separate the pair of capsules as well as the capsule train, which can be further evidenced from the analysis of the time evolution of the capsule velocity inside the corner region.

We believe that the present work is a step forward towards providing practical guidelines to avoid capsule breakup in inertial and non-inertial microfluidic experiments. Inertial particle microfluidics, a technique of increasing interest in the field of biotechnologies, is influenced by several critical factors, including confinement ratio, viscosity ratio, capsule shape, and membrane properties. The current study narrows its focus to the study of spherical capsules, specifically those with a unity viscosity ratio flowing in a small confinement ratio channel. This targeted approach allows for an in-depth exploration of these key parameters under controlled conditions, laying a solid foundation for understanding fundamental microfluidic dynamics. Future works could study capsule membranes exhibiting a strain-hardening elastic behavior, e.g., as described by the Skalak law [52], as well as vary the confinement ratio $\beta = 2\tilde{a}/\tilde{W}$ to consider high-throughput microfluidic devices. In the case of lower confinement ratios in particular, we expect to see stronger capsule interactions along with cross-stream capsule migration inside and downstream of the corner. Finally, the present work could also be useful to develop membrane characterization techniques, where viscoelastic membrane properties could be inferred from the time-dependant evolution of a capsule of interest through a corner.

ACKNOWLEDGMENTS

The authors greatly appreciate the financial support of the Natural Sciences and Engineering Research Council of Canada (NSERC) via Anthony Wachs' New Frontiers in Research Fund Grant No. NFRFE-2018-01922 and Discovery Grant No. RGPIN-2022-03114. Guodong Gai expresses his gratitude to the Pacific Institute of Mathematical Sciences for their support via his 2022–2024 PIMS-CNRS postdoctoral fellowship. This research was enabled by support provided by Digital Research Alliance of Canada [53] through Anthony Wachs's 2022 and 2023 Computing Resources

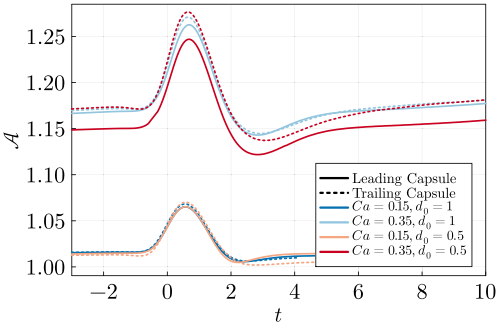

(a) $Re = 0.01$

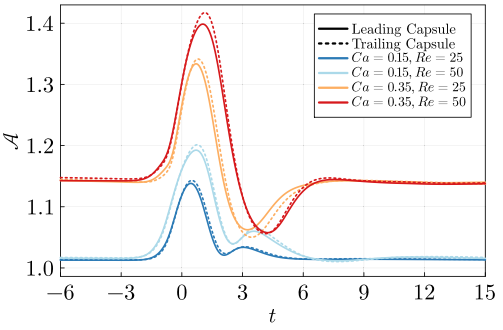

(b) $d_0 = 1$

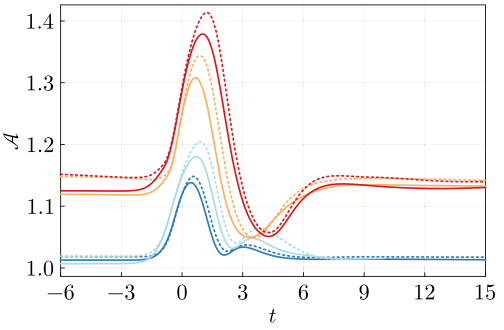

(c) $d_0 = 0.25$

FIG. 22. Temporal evolution of the reduced surface area $\mathcal{A}$ of the leading and the trailing capsules at various interspacings d_0 and various Capillary and Reynolds numbers Ca and Re.

for Research Groups allocation qpf-764-ac. This research was also supported in part through computational resources and services provided by Advanced Research Computing at the University of British Columbia [54].

APPENDIX A: TIME EVOLUTION OF CAPSULE SURFACE AREAS IN THE CASE OF TWO INTERACTING CAPSULES

Figure 22 shows the evolution of the surface area of the leading and the trailing capsules in the non-inertial regime [Fig. 22(a)], as well as at Re = 25 and Re = 50 where the initial interspacing d_0 is 1 [Fig. 22(b)] and 0.25 [Fig. 22(c)].

APPENDIX B: TRAIN OF CAPSULES AT LARGE INITIAL INTERSPACINGS

We provide in Fig. 23 the time evolution of the surface area and velocity of each capsule in a train of 10 capsules flowing through a corner at Re = 50, Ca = 0.35 and a reduced initial interspacing distance between each capsule $d_0 = 0.125$. As can be noted in this figure, the capsules in this regime do not interact as the surface area and velocity evolution of each capsule is almost identical.

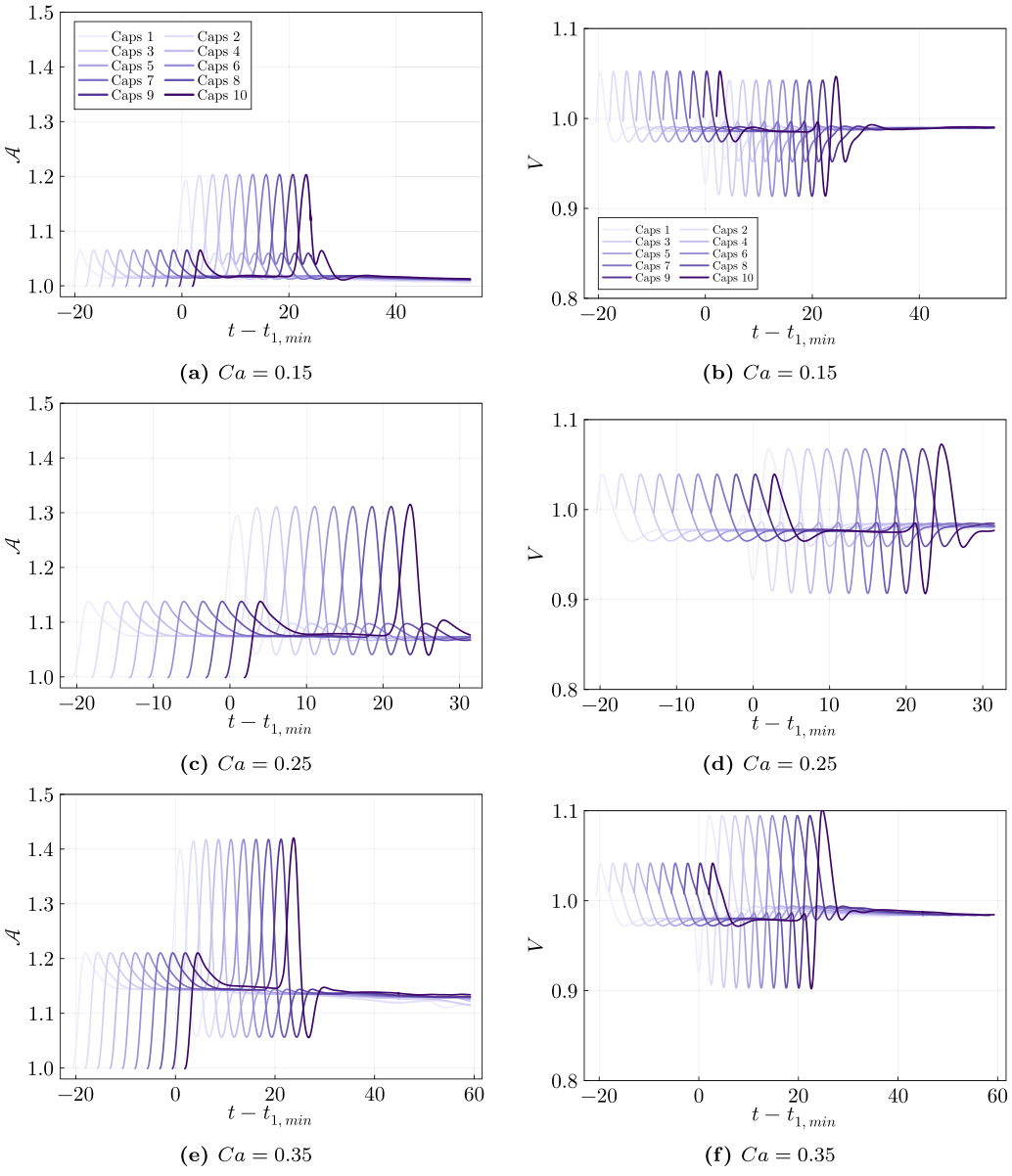

(a) $Ca = 0.15$ **(b)** $Ca = 0.15$

(c) $Ca = 0.25$ **(d)** $Ca = 0.25$

(e) $Ca = 0.35$ **(f)** $Ca = 0.35$

FIG. 23. Time evolution of the reduced surface areas and velocities of a train of ten capsules at Re = 50 and $d_0 = 1$ for Ca = 0.15, 0.25, and 0.35.

[1] D. Barthes-Biesel, Motion and deformation of elastic capsules and vesicles in flow, Annu. Rev. Fluid Mech. **48**, 25 (2016).

[2] Y. H. Bae and K. Park, Targeted drug delivery to tumors: Myths, reality, and possibility, J. Contr. Release **153**, 198 (2011).

[3] P. Kumari, B. Ghosh, and S. Biswas, Nanocarriers for cancer-targeted drug delivery, J. Drug Targeting **24**, 179 (2016).

[4] L. Zhu, C. Rorai, D. Mitra, and L. Brandt, A microfluidic device to sort capsules by deformability: A numerical study, Soft Matter **10**, 7705 (2014).
[5] E. Häner, D. Vesperini, A.-V. Salsac, A. Le Goff, and A. Juel, Sorting of capsules according to their stiffness: From principle to application, Soft Matter **17**, 3722 (2021).
[6] E. Häner, M. Heil, and A. Juel, Deformation and sorting of capsules in a T junction, J. Fluid Mech. **885**, A4 (2020).
[7] Y. Fang, S. Zhu, W. Cheng, Z. Ni, and N. Xiang, Efficient bioparticle extraction using a miniaturized inertial microfluidic centrifuge, Lab Chip. **22**, 3545 (2022).
[8] Z. Wang, Y. Sui, A.-V. Salsac, D. Barthès-Biesel, and W. Wang, Motion of a spherical capsule in branched tube flow with finite inertia, J. Fluid Mech. **806**, 603 (2016).
[9] Z. Wang, Y. Sui, A.-V. Salsac, D. Barthès-Biesel, and W. Wang, Path selection of a spherical capsule in a microfluidic branched channel: Towards the design of an enrichment device, J. Fluid Mech. **849**, 136 (2018).
[10] R. Lu, Z. Wang, A.-V. Salsac, D. Barthès-Biesel, W. Wang, and Y. Sui, Path selection of a train of spherical capsules in a branched microchannel, J. Fluid Mech. **923**, A11 (2021).
[11] J. Gubspun, P.-Y. Gires, C. D. Loubens, D. Barthes-Biesel, J. Deschamps, M. Georgelin, M. Leonetti, E. Leclerc, F. Edwards-Lévy and A.-V. Salsac, Characterization of the mechanical properties of cross-linked serum albumin microcapsules: Effect of size and protein concentration, Colloid Polym. Sci. **294**, 1381 (2016).
[12] T. Lin, Z. Wang, R. Lu, W. Wang and Y. Sui, A high-throughput method to characterize membrane viscosity of flowing microcapsules, Phys. Fluids **33**, 011906 (2021).
[13] Z. Wang, R. Lu, W. Wang, F. Tian, J. Feng and Y. Sui, A computational model for the transit of a cancer cell through a constricted microchannel, Biomech. Model. Mechanobiol. **22**, 1129 (2023).
[14] Z. Zhu, D. Wu, S. Li, Y. Han, N. Xiang, C. Wang, and Z. Ni, A polymer-film inertial microfluidic sorter fabricated by jigsaw puzzle method for precise size-based cell separation, Analytica Chimica Acta **1143**, 306 (2021).
[15] A. E. Green and J. E. Adkins, *Large Elastic Deformations and Non-linear Continuum Mechanics* (Oxford University Press, Oxford, UK, 1960).
[16] D. Barthes-Biesel and J. Rallison, The time-dependent deformation of a capsule freely suspended in a linear shear flow, J. Fluid Mech. **113**, 251 (1981).
[17] C. Pozrikidis, Finite deformation of liquid capsules enclosed by elastic membranes in simple shear flow, J. Fluid Mech. **297**, 123 (1995).
[18] S. Ramanujan and C. Pozrikidis, Deformation of liquid capsules enclosed by elastic membranes in simple shear flow: Large deformations and the effect of fluid viscosities, J. Fluid Mech. **361**, 117 (1998).
[19] C. Pozrikidis, Effect of membrane bending stiffness on the deformation of capsules in simple shear flow, J. Fluid Mech. **440**, 269 (2001).
[20] C. Pozrikidis, Numerical simulation of the flow-induced deformation of red blood cells, Ann. Biomed. Eng. **31**, 1194 (2003).
[21] X.-Q. Hu, B. Sévénié, A.-V. Salsac, E. Leclerc, and D. Barthès-Biesel, Characterizing the membrane properties of capsules flowing in a square-section microfluidic channel: Effects of the membrane constitutive law, Phys. Rev. E **87**, 063008 (2013).
[22] S.-Y. Park and P. Dimitrakopoulos, Transient dynamics of an elastic capsule in a microfluidic constriction, Soft Matter **9**, 8844 (2013).
[23] P. Balogh and P. Bagchi, A computational approach to modeling cellular-scale blood flow in complex geometry, J. Comput. Phys. **334**, 280 (2017).
[24] P. Balogh and P. Bagchi, Analysis of red blood cell partitioning at bifurcations in simulated microvascular networks, Phys. Fluids **30**, 051902 (2018).
[25] P. Balogh and P. Bagchi, The cell-free layer in simulated microvascular networks, J. Fluid Mech. **864**, 768 (2019).
[26] T. Krüger, B. Kaoui, and J. Harting, Interplay of inertia, and deformability on rheological properties of a suspension of capsules, J. Fluid Mech. **751**, 725 (2014).

[27] B. Owen, K. Kechagidis, S. Bazaz, R. Enjalbert, E. Essmann, C. Mallorie, F. Mirghaderi, C. Schaaf, K. Thota, R. Vernekar, Q. Zhou, M. Warkiani, H. Stark, and T. Krüger, Lattice-boltzmann modelling for inertial particle microfluidics applications—A tutorial review, Adv. Phys. X **8**, 1 (2023).
[28] M. Dhar, E. Pao, C. Renier, D. E. Go, J. Che, R. Montoya, R. Conrad, M. Matsumoto, K. Heirich, M. Triboulet, J. Rao, S. S. Jeffrey, E. B Garon, J. Goldman, N. P Rao, R. Kulkarni, E. Sollier-Christen, and D. Di Carlo, Label-free enumeration, collection, and downstream cytological, and cytogenetic analysis of circulating tumor cells, Sci. Rep. **6**, 35474 (2016).
[29] J. Yin, Z. Wang, G. Li, F. Lin, K. Shao, B. Cao, and Y. Hou, Characterization of circulating tumor cells in breast cancer patients by spiral microfluidics, Cell Biol. Toxicol. **35**, 59 (2019).
[30] V. C Ramani, C. A Lemaire, M. Triboulet, K. M Casey, K. Heirich, C. Renier, J. G. Vilches-Moure, R. Gupta, A. M Razmara, H. Zhang, G. W Sledge, E. Sollier, and S. S Jeffrey, Investigating circulating tumor cells, and distant metastases in patient-derived orthotopic xenograft models of triple-negative breast cancer, Breast Cancer Res. **21**, 98 (2019).
[31] J. Son, R. Samuel, B. K Gale, D. T Carrell, and J. M Hotaling, Separation of sperm cells from samples containing high concentrations of white blood cells using a spiral channel, Biomicrofluidics **11**, 054106 (2017).
[32] C. Petchakup, H. M Tay, K. H. H Li, and H. W Hou, Integrated inertial-impedance cytometry for rapid label-free leukocyte isolation, and profiling of neutrophil extracellular traps (NETs), Lab Chip **19**, 1736 (2019).
[33] H. Amini, W. Lee, and D. Di Carlo, Inertial microfluidic physics, Lab Chip **14**, 2739 (2014).
[34] S. K. Doddi and P. Bagchi, Effect of inertia on the hydrodynamic interaction between two liquid capsules in simple shear flow, Int. J. Multiphase Flow **34**, 375 (2008).
[35] A. Kilimnik, W. Mao, and A. Alexeev, Inertial migration of deformable capsules in channel flow, Phys. Fluids **23**, 123302 (2011).
[36] A. H Raffiee, S. Dabiri, and A. M Ardekani, Elasto-inertial migration of deformable capsules in a microchannel, Biomicrofluidics **11**, 064113 (2017).
[37] S. Ebrahimi and P. Bagchi, Inertial, and non-inertial focusing of a deformable capsule in a curved microchannel, J. Fluid Mech. **929**, A30 (2021).
[38] L. Zhu and L. Brandt, The motion of a deforming capsule through a corner, J. Fluid Mech. **770**, 374 (2015).
[39] D. P Huet, http://basilisk.fr/sandbox/huet (2022).
[40] W. Helfrich, Elastic properties of lipid bilayers: Theory, and possible experiments, Z. Naturforschung C **28**, 693 (1973).
[41] Ou-Yang Zhong-Can, and W. Helfrich, Bending energy of vesicle membranes: General expressions for the first, second, and third variation of the shape energy, and applications to spheres, and cylinders, Phys. Rev. A **39**, 5280 (1989).
[42] C. Pozrikidis, *Computational Hydrodynamics of Capsules and Biological Cells* (CRC Press, Boca Raton, FL, 2010).
[43] C. Pozrikidis, Resting shape, and spontaneous membrane curvature of red blood cells, Math. Med. Biol. **22**, 34 (2005).
[44] A. Z. K. Yazdani and P. Bagchi, Phase diagram, and breathing dynamics of a single red blood cell, and a biconcave capsule in dilute shear flow, Phys. Rev. E **84**, 026314 (2011).
[45] D. P. Huet and A. Wachs, A cartesian-octree adaptive front-tracking solver for immersed biological capsules in large complex domains, J. Comput. Phys. **492**, 112424 (2023).
[46] S. Popinet, A quadtree-adaptive multigrid solver for the Serre–Green–Naghdi equations, J. Comput. Phys. **302**, 336 (2015).
[47] C. Peskin, Numerical analysis of blood flow in the heart, J. Comput. Phys. **25**, 220 (1977).
[48] C. Peskin, The immersed boundary method, Acta Numer. **11**, 479 (2002).
[49] D. V Le, Effect of bending stiffness on the deformation of liquid capsules enclosed by thin shells in shear flow, Phys. Rev. E **82**, 016318 (2010).

[50] M. Uhlmann, An immersed boundary method with direct forcing for the simulation of particulate flows, J. Comput. Phys. **209**, 448 (2005).
[51] S. Ebrahimi, P. Balogh, and P. Bagchi, Motion of a capsule in a curved tube, J. Fluid Mech. **907**, A28 (2021).
[52] R. Skalak, A. Tozeren, R. Zarda, and S. Chien, Strain energy function of red blood cell membranes, Biophys. J. **13**, 245 (1973).
[53] https://alliancecan.ca/en.
[54] https://arc.ubc.ca/.